Thermodynamic analysis and economic assessment of a carbon dioxide hydrate-based vapor compression refrigeration system using load shifting controls in summer

Citation for published version:
Hua, N, Lu, T, Yang, L, McKeown, A, Yu, Z, Xu, B, Sciacovelli, A, Ding, Y & Li, Y 2022, 'Thermodynamic analysis and economic assessment of a carbon dioxide hydrate-based vapor compression refrigeration system using load shifting controls in summer', *Energy Conversion and Management*, vol. 251, 114901. https://doi.org/10.1016/j.enconman.2021.114901

Digital Object Identifier (DOI):
10.1016/j.enconman.2021.114901

Link:
Link to publication record in Heriot-Watt Research Portal

Document Version:
Peer reviewed version

Published In:
Energy Conversion and Management

Thermodynamic analysis and economic assessment of a carbon dioxide hydrate-based vapor compression refrigeration system using load shifting controls in summer

Nan Hua[1], Tiejun Lu[1], Liwei Yang[2], Andrew Mckeown[3], Zhibin Yu[3], Bing Xu[4], Adriano Sciacovelli[1], Yulong Ding[1], Yongliang Li[1*]

[1] School of Chemical Engineering, University of Birmingham, Birmingham, B15 2TT, United Kingdom,
[2] School of Engineering and Materials Science, Queen Mary University of London, London, E1 4NS, United Kingdom,
[3] James Watt School of Engineering, University of Glasgow, Glasgow, G12 8QQ, United Kingdom,
[4] Department of Accountancy, Economics and Finance, Heriot-Watt University, Edinburgh, EH14 4AS, UK

Abstract

The present work proposed a novel two-stage carbon dioxide hydrate-based vapor-compression refrigeration system. The proposed system applied pure carbon dioxide hydrate as the primary refrigerant and arranged both of hydrate formation and dissociation at the low-pressure stage. The thermodynamic and economic models were developed and then performances of the proposed system using load-levelling storage and full storage operations were evaluated and compared with those of a conventional carbon dioxide single-stage vapor-compression refrigeration system, which is treated as the baseline and with no energy storage. The simulation results indicate that the design capacity of the proposed system using full storage is the largest among the three systems, but with lowest operation cost, and with the incentivization of electricity prices ratio of on and off-peak this cost savings would raise significantly. Noted that the bill structure reveals the load-levelling storage system saves most on the water consumption. Due to the dominant expenditure on the two compressors, compare with the baseline

1, *Corresponding author: Tel: +44 (0)121 414 5135
E-mail y.li.1@bham.ac.uk

system, the initial capital cost of the full storage system was 75.5% higher, whereas that of the levelling-load storage system was only 21.5% higher. Finally, this paper discussed the economic feasibility on the initial capital cost for the proposed system and developed an indication map to predict the profit years in case of that the new system using load-levelling storage operation replaces the baseline system assuming a system lifetime of 15 years under different electricity prices ratios.

Keywords: Two-stage compression; Carbon dioxide hydrate; Cold energy storage; Load shifting strategy; Thermo-economics

Nomenclature

a	subcooling degree
A	surface area (m^2)
C	cost (£) or cycle of concentration of cooling tower
CFR	capital recovery factor
COP	coefficient of performance
Cp	specific heat ($J\ kg^{-1}\ K^{-1}$)
d	diameter (m)
D_c	fin collar outside diameter (m)
D_h	hydraulic diameter (m)
e	electricity tariff (pence kWh^{-1})
E	evaporation loss ($kg\ s^{-1}$)
f	frequency (Hz) or friction factor
F_p	fin pitch (m)
GWP	global warming potential

h	enthalpy (J kg^{-1}) or heat transfer coefficient (W m^{-2} K^{-1})
i	segment index
j	the Coburn factor
l	length (mm)
k	thermal conductivity (W m^{-1} K^{-1})
$LMTD$	log mean temperature difference (K)
m	mass flow rate (kg s^{-1})
N	number of tube row
NTU	number of transfer unit
Nu	Nusselt number
ODP	ozone depletion potential
P	pressure (kPa)
P_{l}	longitudinal tube pitch
Pr	Prandtl number
P_{t}	transverse tube pitch
Q	heat transfer rate (W)
r	ratio of mass flow rate in high- and low-stages
Re	Reynolds number
T	temperature (°C)
U	overall heat transfer coefficient (W m^{-2} K^{-1})
V	volume (m^3)
W	power consumption (kW)
X_{tt}	Lockhart-Martinelli parameter

Greek symbols

α	heat transfer coefficient (W m^{-2} K^{-1})
ε	effectiveness
Δ	difference
η	efficiency
μ	dynamic viscosity (kg $m^{-1}s^{-1}$)
ρ	density (kg m^{-3})
σ	surface tension (N m^{-1})
ϕ	relative humidity
χ	vapor quality
ω	capacity flow ratio

Subscripts

a	air
atm	atmospheric
b	bulk
b_down	blow-down
cap	capital
ct	cooling tower
comp	compressor
db	dry-bulb
dec	carbon dioxide hydrate decomposer
diff	difference
E	electricity
eval	expansion valve
evap	evaporator

ex	exit
f	film temperature
fic	fictitious
gc	gas cooler
H	high-stage
hyd	hydrate
i	inner
I	intermediate-stage
in	inlet
isen	isentropic
l	liquid
L	low-stage
m_up	make-up
min	minimum
mix	mixture
nom	nominal
o	outer
out	outlet
op	operation
r	ratio
rev	revolution
sat	saturation
su	supply
tot	total
v	vapor

V	vapor
vol	volumetric
w	water
wb	wet-bulb

Acronyms

CHB-VCRS	carbon dioxide hydrate-based vapor-compression refrigeration system
CTES	cold thermal energy storage
FS	full storage
LS	load-levelling storage
PCM	phase change material
SC-VCRS	single-stage carbon dioxide vapor-compression refrigeration system
VCRS	vapor-compression refrigeration system

1. Introduction

Nowadays, fossil fuel, as the most important energy source, generates around 70-80% of the total world electricity. The continuous and excessive combustion of fossil fuel already causes a series of serious environmental problems, such as global warming and climate change. This situation deteriorates with the significant rising in electricity consumption. Coulomb et al. [1] pointed it out that more than 17% of total electric demands is from the air-conditioning and refrigeration sector, whereas a considerable portion of which is consumed during the peak-load hours. Under such a background, the development of high-efficiency refrigeration system and peak-load shift methods matched will effectively save the additional fossil fuel used to generate electricity which in turn, helps to reduce carbon emissions and minimize environmental impact.

Advanced refrigeration system incorporating cold thermal energy storage (CTES) technology is one of the most promising options. The CTES is one of effective manners dealing with peak-load shift. Mosaffa et al. [2] developed an air conditioning system consisting of a combination of latent heat thermal storage and vapor-compression refrigeration. It produces and stores the cooling capacity during nighttime, and utilizes the stored cooling capacity for air conditioning during daytime, which significantly reduces the electricity demand during the peak-load period. During the cold storing process in this combined system, the air in duct as the secondary refrigerant is extracted heat by the primary refrigerant (1,1,1,2-tetrafluoroethane (HFC-134a)) of the vapor-compression refrigeration system (VCRS), and then cools down and stores cold energy into the phase change materials (PCMs). As a process of indirect cooling, such a refrigeration system requires additional components and generates extra exergy losses. Therefore, a substance, which could be both the primary refrigerant and PCM would be viable in developing a high-efficiency and economic refrigeration system incorporating CTES.

As for one method of solution, refrigerant gas hydrate could be the one. Clathrate hydrates are crystalline solid consisting of water molecular cavities and refrigerant gas guested molecules. The research on refrigerant gas hydrates applied to CTES systems started in the 1980s [3] since the thermodynamic properties are suitable for refrigeration applications (high dissociation enthalpy, low pressure and wide temperature range). For instance, the studies of Mori and Mori [4] focused on the injection of a refrigerant fluid (trichlorofluoromethane (CFC-11), chlorodifluoromethane (HCFC-22) and HFC-134a) into water stored in a direct-contact crystallizer and form clathrates during cold storing, later the clathrate melted to produce chilled water. This process was not a continuous and enclosed cycle. Recently, Ogawa et al. [5] proposed a novel conceptual design of a refrigeration system using , refrigerant gas hydrates as the primary refrigerant. The novel system can provide superior performance.. Different from a conventional VCRS, evaporation and condensation are replaced by hydrate dissociation and formation. Between those, a multiphase (guest gas and liquid water) compression occur in this hydrate-based system. One of the notable hydrate properties is that the heat of formation/dissociation is generally several times as large as the latent heat of the conventional refrigerants. For instance, the enthalpy of dissociation of carbon dioxide (CO_2) hydrate is reported to be 80 kJ mol^{-1} [6], whereas CO_2 enthalpy of evaporation is only 18 kJ mol^{-1} [7]. There are two basic principles of selection of the hydrate-forming guest refrigerant gas. One is that the environment-friendly gases are preferred. The other is that the formation/dissociation pressure should be relatively low (less than 5 MPa) at the temperature of the application scenarios, usually between the range of 278-303 K [8].

Only a few publications reported the research on the hydrate-based refrigeration system. Ogawa et al. [5] proposed the conceptual design and developed a numerical modelling of an innovative hydrate-based refrigeration cycle using the hydrate of difluoromethane (HFC-32)/cyclopentane (CP) guest pair. 0.03/1.67 MPa and 7.5/27 °C were the design conditions at the low and high stages. The coefficient of performance (COP) of the system reached as high as 8.0. A laboratory-scale prototype system was constructed and steadily operated for two hours. Zhang et al. [9] conducted the comparison of three types of hydrate-based refrigeration systems using Aspen Plus. One is multiphase compression cycle and the other two are vapor compression cycles. Two-group conditions of (0.336/2.988 MPa and 293.0/305.9 K) and (0.206/2.051 MPa and 293.3/306.2 K) were selected for the two hydrates of methyl fluoride (HFC-41)/CP and HFC-41/monofluo cyclopentane (FCP), respectively. Their results demonstrated that the highest COP was 8.01-8.97, which was 2-4 times of those of the conventional vapor-compression refrigeration system. Matsuura et al. [7] developed a thermodynamic model to clarify the dominant factor to influence COP. 287 K and 297 K were set as the low and high temperatures for dissociation and formation. 0.139-0.234 MPa and 0.787-1.733 MPa are the pressure variation ranges at the low and high stages. The maximum COP values of the three hydrate-based systems including HFC-32/CP/water, Kr/CP/water and HFC-41/CP/water were 18.22, 18.66 and 14.03, respectively. Their calculated results revealed that the dissociation heat of the hydrates and the enthalpy change of guest gas were the dominant factors. HFC-32 and HFC-41 have no ozone depletion potential (ODP), but considerable global warming potential (GWP). Kr is the natural gas but only 0.000114 vol.% of the atmosphere. Thus, as an ideal guest refrigerant gas forming the hydrate with attractive properties include no ODP, very low GWP, non-flammable, non-toxic and low-cost is desired. CO_2 is then becoming one of the popular guest gases. Xie et al. [10] had made their efforts to develop a mixed CO_2 hydrate-based vapor-compression refrigeration system (CHB-VCRS). Normally, pure CO_2 hydrate is formed under high pressure and low temperature [11]. They used tetrahydrofuran (THF) as the thermodynamics promoter to alleviate the equilibrium formation pressure. 0.25/3.0 MPa and 280/292 K were chosen as the design conditions. The simulated results showed that the COP of the system was obtained as high as 6.8, and would be decreased by 30 % when the formation temperature only raised by 5 K.

All refrigerant hydrate-based refrigeration systems are actually CTES systems. The formation heat exchanger (a crystallizer such as a condenser, or a vessel) also plays a role of a cold energy storage vessel. As depicted by Xie et al. [10], in CBHS-VCRS, the CO_2 gases discharged from the compressor are injected into a crystallizer, and then the cold energy is stored via the clathrates forming during the off-peak period. Later the hydrate slurries are expanded via a slurry pump and directly delivered to the users (heat exchangers such as evaporators) during the on-peak period. In addition, those typical energy storage strategies widely used in conventional CTESs [12], such as full storage, load-levelling storage and partial storage, still can be applied to the novel hydrate-based refrigeration systems. Xie et al. [10] investigated a CHB-VCRS with CTES under two operation strategies, i.e., full storage and load-levelling storage for an office room and a storeroom. The former one was adopted by using the hourly energy storage, and the latter one chose the monthly cold storage. The peak load of the storeroom in the hottest month was cut by 22% but facing a huge initial investment on the storage tank. Zhou et al. [13] modeled and experimented a fluidized bed based CTES system with a variable cooling load in the summer of the Netherlands. The CO_2 hydrates were used as PCMs. The energy efficiency of this CTES system with nighttime production was improved by 23%-43% compared with the conventional system. At the meantime, the investment costs of the hydrate slurry tank were notably reduced. In addition to common indicators, such as cooling load, power consumption and life cycle cost (summation of initial capital cost and operation cost) [14], environmental considerations need also be included in evaluation of a CHB-VCRS incorporating CTES technologies. For instance, Dai et al introduced a life cycle climate performance to indicate the CO_2 emissions of the CO_2 system over the whole lifetime [15], an indicator including pollution emissions to express the environmental performance for different strategies [16].

In summary, the CO_2 hydrate-based refrigeration systems existed in literature have two characteristics: 1) the formation and dissociation are arranged at the high-pressure (condensation) and low-pressure (evaporation) stages; 2) the formation and dissociation pressure should be relatively low at the temperature of the application scenarios. The first one brings the high initial investment, complex configuration and low system reliability, due to the multi-phase compressor (or vapor compressor plus water pump) and the slurry pump. The second one increases the difficulty and cost of preparation of mixed CO_2 hydrate. Therefore, in this work, a two-stage CHB-VCRS using pure CO_2 hydrate was proposed. The equilibrium pressures of formation and dissociation have the same level. Thus both of them can be arranged at the low-pressure stage, which only need simplified reform at the evaporation side for the conventional VCRS This created the feasibility for the improvement of the proposed CHB-VCRS system performance by applies existed advanced technologies of conventional VCRS, such as the two-stage compression. In addition, the exothermic reaction of CO_2 hydrate generated in a reactor of the proposed system was cooled by the two-phase CO_2 injected itself, rather than extra external cooling. The present work develop the numerical model of the proposed system and applies it to conduct the thermodynamic and economic analyses. A comparison of CHB-VCRS and conventional single-stage CO_2 vapor-compression (SC-VCRS, the baseline) considering different CTES operation strategies and different time-of-use electricity tariffs is implemented. In the end, this paper summarized the results of all these efforts and discussed the potential feasibility of new CHB-VCRSs to replace the conventional SC-VCRS.

2. Description of carbon dioxide hydrate-based vapor-compression refrigeration system

As depicted in Fig. 1(a), a two-stage cycle is adopted for the present CHB-VCRS, aiming to reduce the compressor discharge temperature. The thermodynamic processes of the cycle are given in Fig. 1(b). The whole system is divided into three substages: the high-pressure stage, the saturated-vapor CO_2 (State 6) is inhaled to a high-pressure stage compressor and becomes supercritical state (State 7). Then it is cooled and reaches the pseudo-critical temperature at the exit of the gas-cooler (State 1). Finally, a portion of CO_2 out of the gas-cooler experiences a subcooling during a coil submerging inside a flash tank (State 2) and goes into the tank reactor; the intermediate-pressure stage, the remaining portion CO_2 from the gas-cooler becomes two-phase (State 8) undergoing an expansion process and then is delivered into the flash tank directly. The liquid CO_2 cools the coil and vaporizes to be saturated vapor state (State 6). In addition, a portion of superheated vapor CO_2 discharged from a low-stage compressor is cooled by the liquid CO_2 to be saturated vapor state (State 6) in the flash tank as well. All the saturated vapor CO_2 at State 6 is provided to the high-stage compressor; and lastly, the low-pressure stage, where the CO_2 hydrates are formatted in a tank reactor. Different from the conventional hydrate-based refrigeration system, there is no external cooling mediate supplied to the formation tank, such as a bubble column reactor. The two-phase CO_2 (State 3) with low temperature and low pressure injected into the aqueous solution via a nozzle, not only provides gas source for CO_2 hydrate formation, but also absorbs the heat from the exothermic hydration reaction. The redundant saturated-vapor CO_2 is discharged from the port at the top of the tank and delivered to the low-stage compressor. The CO_2 hydrate slurry is pumped to a heat exchanger to melt and then the mixture of water and vapor CO_2 go through a liquid-vapor separator. Water is circulated back to the tank reactor for reusing and the saturated-vapor CO_2 (State 4) is compressed by the low-stage compressor together with saturated-vapor CO_2 from the reactor. Moreover, the cooling tower supplies the enough cooling water to reduce the operating temperature in the gas cooler.

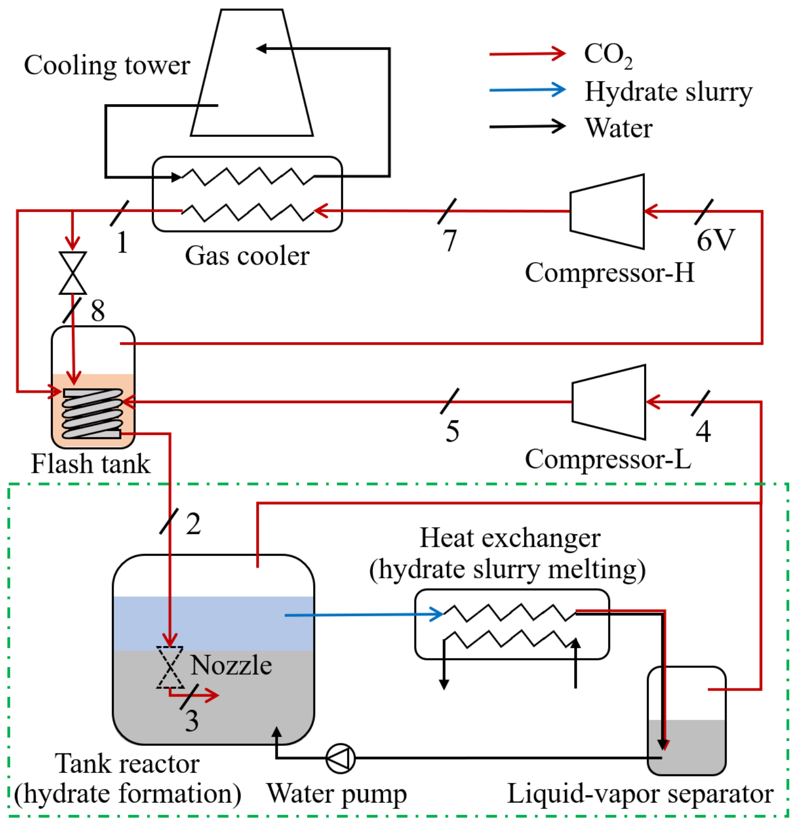

(a)

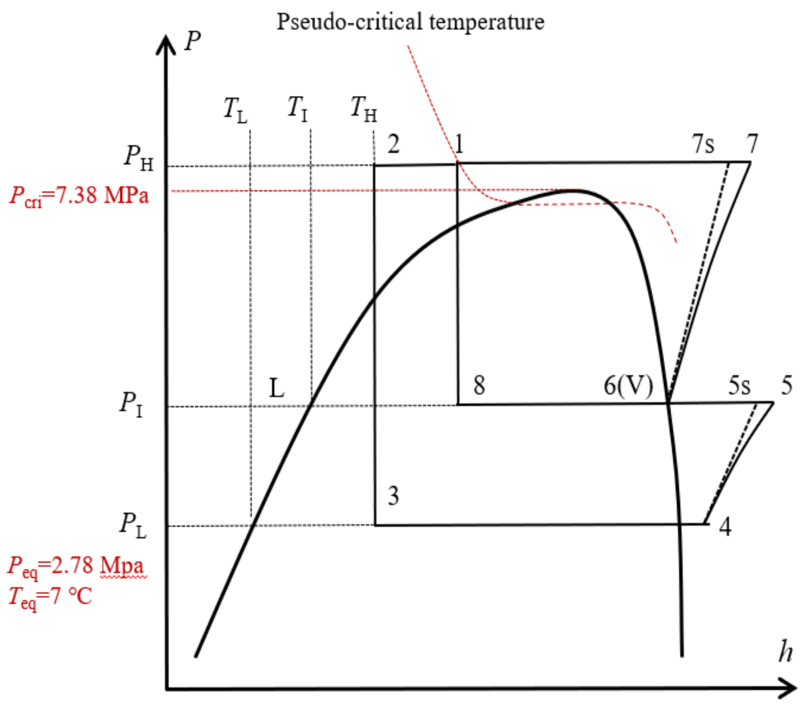

(b)

Figure 1 Schematic and P-h diagram of CHB-VCRS

The two-stage CHB-VCRS is characterized as follows. The pressure losses in all components and pipelines are negligible. Equations (1a) and (1b) expresses the balance of mass flow rates and their ratio at high-stage and low-stage, which significantly affect the system performance.

$$m_{\mathrm{CO_2,H}} = m_{\mathrm{CO_2,I}} + m_{\mathrm{CO_2,L}}, \quad m_{\mathrm{CO_2,H}} \geq m_{\mathrm{CO_2,L}} \tag{1a}$$

$$r = \frac{m_{\mathrm{CO_2,H}}}{m_{\mathrm{CO_2,L}}} \tag{1b}$$

A subcooling parameter, *a*, is defined by Torrella et al. [17] to indicate the sub-cooler effectiveness in the flash tank, as expressed by Eq. (2). It is noted that h_{L} is the enthalpy of saturated liquid CO_2 (State L) at intermediate pressure.

$$a = \frac{h_1 - h_2}{h_1 - h_{\mathrm{L}}} \quad (0 \leq a \leq 1) \tag{2}$$

In addition, the energy balance of the inter-pressure stage can be expressed by Eq. (3). Taking into account Eqs. (1-2), the mass flow ratio, *r*, can be derived based on the subcooling parameter, *a*, by Eq. (4):

$$m_{\mathrm{CO_2,L}} h_1 + m_{\mathrm{CO_2,I}} h_1 + m_{\mathrm{CO_2,L}} h_5 = m_{\mathrm{CO_2,H}} h_{6(\mathrm{V})} + m_{\mathrm{CO_2,L}} h_2 \tag{3}$$

$$r = \frac{h_5 - h_1 + a(h_1 - h_{\mathrm{L}})}{h_{6(\mathrm{V})} - h_1} \tag{4}$$

In the present work, the CHB-VCRS provides the hydrate slurries which generate and melt at the equilibrium temperature of 7 °C. Assume that there is no pressure drop during hydrate formation and dissociation, the low-stage pressure equals to the corresponding equilibrium pressure, 2.78 MPa. Figure 2 (a) illustrates the variation of the mass flow ratio, *r*, as function of the subcooling parameter, *a*, at different inter-stage pressures, P_{I}, when the high-stage pressure, P_{H}, is fixed at 9 MPa. The intermediate-stage pressure is also an significant parameter for a two-stage compression system. It can be observed that the mass flow ratio, r, increases together with increasing of the subcooling parameter, a, and the intermediate pressure, P_I. Moreover, there is a little sharper increase of the mass flow ratio when the intermediate-stage pressure decreases.

A COP expression, as seen in Eq. (5), can be established using the subcooling parameter, a. The power consumption of the water pump here at low-stage (between the liquid-vapor separator and the tank reactor) is negligible.

$$COP = \frac{h_4 - h_3}{\dfrac{h_{5s} - h_4}{\eta_{\mathrm{isen,L}}} + r \times \dfrac{h_{7s} - h_{6(V)}}{\eta_{\mathrm{isen,H}}}} = \frac{h_4 - h_3}{\dfrac{h_{5s} - h_4}{\eta_{\mathrm{isen,L}}} + \left[\dfrac{h_5 - h_1 + a(h_1 - h_L)}{h_{6(V)} - h_1}\right] \times \dfrac{h_{7s} - h_{6(V)}}{\eta_{\mathrm{isen,H}}}} \tag{5}$$

where $\eta_{\mathrm{isen,L}}$ and $\eta_{\mathrm{isen,H}}$ represent the isentropic efficiency at low-stage and high-stage pressures, respectively.

Actually, the inter-stage pressure, P_I, plays an important role in the optimization of the two-stage system. As depicted in Fig. 2(b), the COP increases with increasing of the subcooling parameter, a, at a fixed inter-stage pressure. As shown in Fig. 1(b), a bigger subcooling means a larger difference in specific enthalpy between the states 3 and 4, and then results in more CO_2 hydrate generated. Moreover, with the increasing of the subcooling parameter, the optimum inter-stage pressure on the basis of maximum COP is moving to the higher value of the inter-stage pressure.

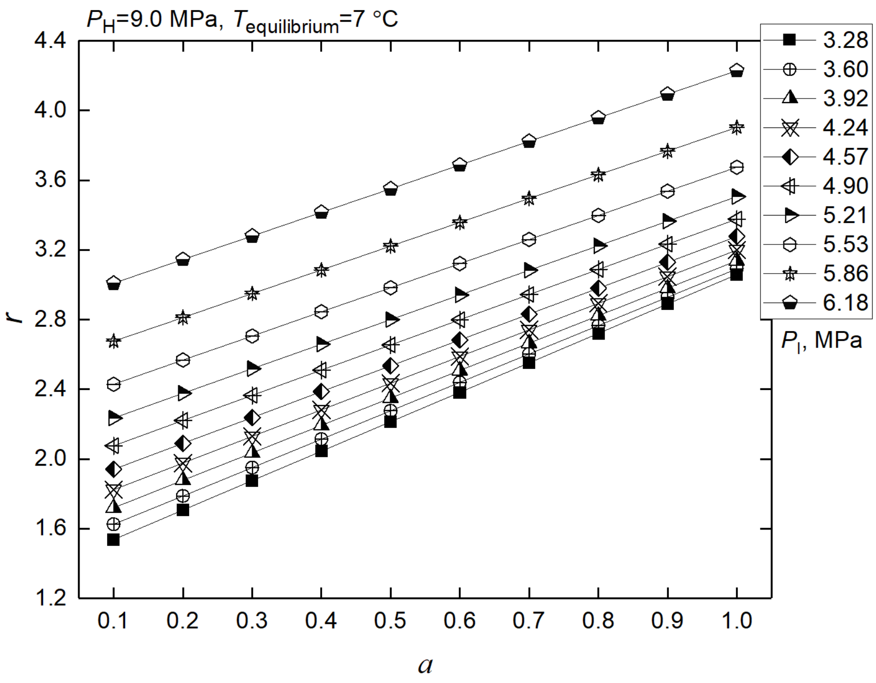

(a)

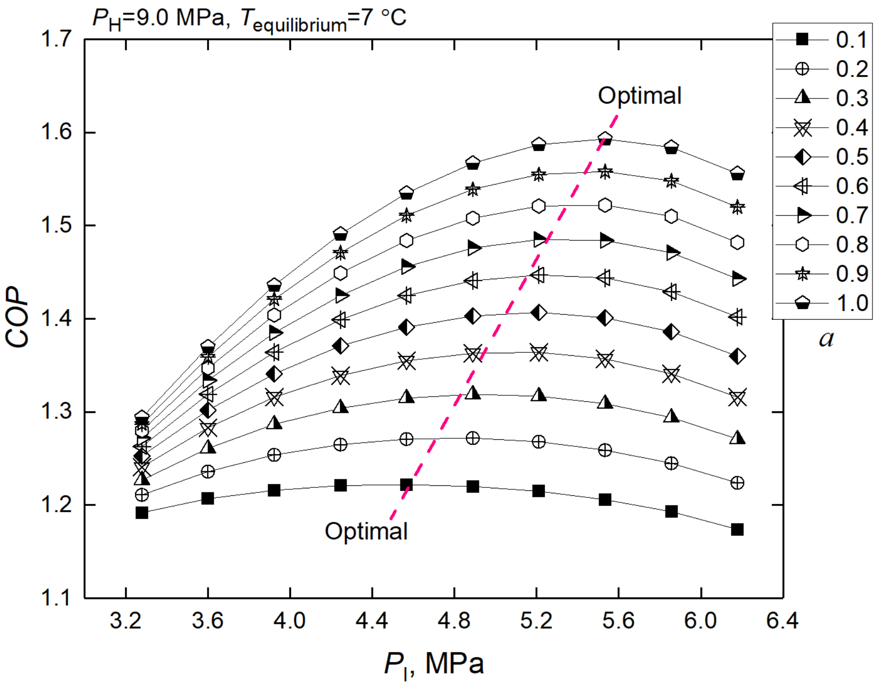

(b)

Figure 2 Schematic and P-h diagram of CO_2 hydrate-based VCR system

3.Mathematical model

The first law of thermodynamic is implemented to each component of the system. There are some assumptions as following:

1) The system is under steady state conditions.
2) The expansion of CO_2 in the nozzle of the reactor is assumed as isenthalpic.
3) The pressure losses in all pipelines and components are negligible.
4) The heat losses in all pipelines and components are negligible.
5) The power consumption of the water pump between the liquid-vapor separator and the tank reactor at low-stage is negligible.

3.1 Gas cooler

Tube-in-tube heat exchanger is selected as the gas cooler. The water flows in the annulus while the CO_2 flows counter-currently along the inner tube. Due to the thermophysical properties of CO_2 dramatically vary with temperature and pressure in the supercritical region, the gas cooler is discretized into a number of small elements. The energy conservation equations are applied in both sides of water and CO_2 in each element. The heat balance can be expressed by the following equations:

$$Q(i) = \dot{m}_{\mathrm{CO_2}}(h_{\mathrm{CO_2}}(i) - h_{\mathrm{CO_2}}(i+1)) = \dot{m}_{\mathrm{w}} Cp_{\mathrm{w}}(i)(T_{\mathrm{w}}(i) - T_{\mathrm{w}}(i+1)) \tag{6a}$$

$$Q(i) = UA(i) \times LMTD(i) \tag{6b}$$

where i refers to the element index along the calculation direction.

The overall heat transfer coefficient is obtained by:

$$\frac{1}{UA(i)} = \frac{1}{h_{\mathrm{w}}(i)A_{\mathrm{o}}} + \frac{\ln\left(d_{\mathrm{o}}/d_{\mathrm{i}}\right)}{2\pi k_{\mathrm{wall}} l} + \frac{1}{h_{\mathrm{CO_2}}(i)A_{\mathrm{i}}} \tag{7}$$

where l is the length of the element.

Table 1 Summary of correlations for heat transfer

Type and source	Equations
CO_2 in gas cooler (Dang and Hihara [18])	$Nu = \dfrac{(f/8)(Re-1000)Pr}{1.07+12.7\,(f/8)^{1/2}(Pr^{2/3}-1)}$ $f = [1.82\log(Re) - 1.64]^{-2}$ $Pr = \begin{cases} Cp_{\mathrm{b}}\mu_{\mathrm{b}}/k_{\mathrm{b}} & \text{for } Cp_{\mathrm{b}} > \bar{C}p \\ \bar{C}p\mu_{\mathrm{b}}/k_{\mathrm{b}} & \text{for } Cp_{\mathrm{b}} < \bar{C}p \ , \mu_{\mathrm{b}}/k_{\mathrm{b}} \geq \mu_{\mathrm{f}}/k_{\mathrm{f}} \\ \bar{C}p\mu_{\mathrm{f}}/k_{\mathrm{f}} & \text{for } Cp_{\mathrm{b}} < \bar{C}p \ , \mu_{\mathrm{b}}/k_{\mathrm{b}} < \mu_{\mathrm{f}}/k_{\mathrm{f}} \end{cases}$ $\bar{C}p = \dfrac{h_{\mathrm{b}} - h_{\mathrm{wall}}}{T_{\mathrm{b}} - T_{\mathrm{wall}}}$
Water in gas cooler (Gnielinsk [19])	$Nu = \dfrac{(f/8)(Re-1000)Pr}{1.07+12.7\,(f/8)^{1/2}(Pr^{2/3}-1)}$ $f = [1.82\log(Re) - 1.64]^{-2}$
Cooling tower (Lebrun and Silva [20])	$AU = 746 m_{\mathrm{w}}^{0.43} m_{\mathrm{a}}^{1.03}$
CO_2 evaporation (Hwang et al. [21])	$\alpha_{\mathrm{cb}} = 0.023 \dfrac{k_{\mathrm{l}}}{D_{\mathrm{h}}} Re_{\mathrm{l}}^{0.8} Pr_{\mathrm{l}}^{0.4}$ $F = \begin{cases} 1 & \text{for } \frac{1}{X_{\mathrm{tt}}} > 0.1 \\ 2.35\left(\frac{1}{X_{\mathrm{tt}}} + 0.213\right)^{0.736} & \text{for } \frac{1}{X_{\mathrm{tt}}} \leq 0.1 \end{cases}$ $\dfrac{1}{X_{\mathrm{tt}}} = \left(\dfrac{\rho_{\mathrm{l}}}{\rho_{\mathrm{v}}}\right)^{0.5} \left(\dfrac{\mu_{\mathrm{v}}}{\mu_{\mathrm{l}}}\right)^{0.1} \left(\dfrac{\chi}{1-\chi}\right)^{0.9}$ $\alpha_{\mathrm{nb}} = 0.00122 \dfrac{k_{\mathrm{l}}^{0.79} Cp_{\mathrm{l}}^{0.45} \rho_{\mathrm{l}}^{0.49}}{\sigma^{0.45} \mu_{\mathrm{l}}^{0.29} \mu_{\mathrm{v}}^{0.24} \Delta h_{\mathrm{v}}} \Delta T_{\mathrm{sat}}^{0.24} \Delta P_{\mathrm{sat}}^{0.75}$ $\Delta P_{\mathrm{sat}} = P_{\mathrm{sat}}(T_{\mathrm{wall}}) - P_{\mathrm{sat}}(T_{\mathrm{sat}})$ and $\Delta T_{\mathrm{sat}} = T_{\mathrm{wall}} - T_{\mathrm{sat}}$ $S = \frac{1-\exp(-\beta)}{\beta}$ with $\beta = \frac{F\alpha_{\mathrm{cb}} X_0}{k_{\mathrm{l}}}$ and $X_0 = 0.05\left[\dfrac{\sigma}{\mathrm{g}(\rho_l - \rho_{\mathrm{v}})}\right]^{0.5}$
Single-phase CO_2 in evaporator (Mac Adams [22])	$Nu = 0.023 Re^{0.8} Pr^{0.4}$
Air in evaporator (Wang et al. 23])	$Nu = jRePr^{1/3}$ $j = 0.086 Re^{P1} N^{P2} \left(\dfrac{F_{\mathrm{P}}}{D_{\mathrm{c}}}\right)^{P3} \left(\dfrac{F_{\mathrm{P}}}{D_{\mathrm{h}}}\right)^{P4} \left(\dfrac{F_{\mathrm{P}}}{P_{\mathrm{t}}}\right)^{0.93}$ $P1 = -0.361 - \dfrac{0.042N}{\log_e(Re)} + 0.158\log_e\left(N\left(\dfrac{F_{\mathrm{P}}}{D_{\mathrm{c}}}\right)^{0.41}\right)$ $P2 = -1.224 - \dfrac{0.042\left(\frac{P_{\mathrm{l}}}{D_{\mathrm{h}}}\right)^{1.42}}{\log_e(Re)}$ $P3 = -0.083 + \dfrac{0.058N}{\log_e(Re)}$ $P4 = -5.735 + 1.21\log_e\left(\dfrac{Re}{N}\right)$

The correlation of the heat transfer coefficient of the supercritical CO_2 in tubes is from Dang and Hihara [18]. The heat transfer coefficient for the water side is obtained via the Gnielinsk correlation [19]. The details can be found in Table 1. In addition, the flowchart of the heat transfer calculation in a segment can be found in Fig. B1.

3.2 Cooling tower

A simplified model of direct contact cooling tower was developed by Lebrun et al. [25]. This model assumed the humid air was replaced by a fictitious perfect gas and the temperature of which is the wet-bulb temperature. Therefore, as depicted in Fig. A1, the wet-bulb temperature of the moist air can be iteratively calculated by Eq. (8).

$$T_{\mathrm{wb}} = T - \frac{p_{\mathrm{sat}}(T_{\mathrm{wb}}) - (\phi_{\mathrm{a}}/100)p_{\mathrm{sat}}(T)}{kp_{\mathrm{atm}}} \quad (8)$$

where k is a constant, p_{atm} is the atmospheric pressure, ϕ_{a} is the relative humidity and $p_{\mathrm{sat}}(T_{\mathrm{wb}})$ and $p_{\mathrm{sat}}(T)$ are the air saturation vapor pressures at T and T_{wb}, respectively.

The energy balance on the air side can be given:

$$Q = \dot{C}_{\mathrm{a,fic}}(T_{\mathrm{wb,ex}} - T_{\mathrm{wb,su}}) = \dot{m}_{\mathrm{a}} Cp_{\mathrm{a,fic}}(T_{\mathrm{wb,ex}} - T_{\mathrm{wb,su}}) \quad (9)$$

where $Cp_{\mathrm{air,fic}}$ defines as a fictitious specific heat by Eq. (10).

$$Cp_{\mathrm{a,fic}} = \frac{(h_{\mathrm{a,ex}} - h_{\mathrm{a,su}})}{(T_{\mathrm{wb,ex}} - T_{\mathrm{wb,su}})} \quad (10)$$

The water flows in counter current arrangement with the air flow in cooling tower, thus the energy balance on the water side can be given by:

$$Q = \dot{C}_{\mathrm{w}}(T_{\mathrm{w,su}} - T_{\mathrm{w,ex}}) = \dot{m}_{\mathrm{w}} Cp_{\mathrm{w}}(T_{\mathrm{w,su}} - T_{\mathrm{w,ex}}) \quad (11)$$

In accordance with the definition of an equivalent heat exchanger for the simulation of the direct contact cooling tower, the heat flow rate can be calculated by Eq. (12). The effectiveness of a counter flow cooling tower is given by Eq. (13).

$$Q=\varepsilon_{\text{fic}}\dot{C}_{\min}(T_{\text{w,su}}-T_{\text{a,wb,su}}) \tag{12}$$

$$\varepsilon_{\text{fic}}=\frac{1-\exp(-NTU_{\text{fic}}(1-\omega))}{1-\omega\exp(-NTU_{\text{fic}}(1-\omega))} \tag{13}$$

The fictitious, NTU_{fic}, is defined in Eq. (14). The fictitious cooling tower heat transfer coefficient, AU_{fic}, is related to the real water-air overall heat transfer coefficient, AU, and the moist air specific heat, Cp_{a}, in Eq. (15).

$$NTU_{\text{fic}}=\frac{AU_{\text{fic}}}{\dot{C}_{\min}} \tag{14}$$

$$AU_{\text{fic}}=AU\frac{Cp_{\text{a,fic}}}{Cp_{\text{a}}} \tag{15}$$

Cp_{a} here is assumed constant and equal to 1025 J kg^{-1} K^{-1} in good approximation (ASHRAE1997 [26]). The real water-air overall heat transfer coefficient for the cooling tower, AU, can be obtained by the correlation (Table 1) of Lebrun and Silva [20]. In addition, the flowchart of the modeling of direct contact cooling tower can be found in Fig. A2.

3.3 Variable-speed Compressor

A model of variable-speed compressor is applied to determinate the mass flow rate, the power consumption and the discharge CO_2 state of the compressor. Equations (16) and (17) are the curve fits by Nguyen and Eslami-Nejad [27] for an open-type CO_2 compressor and used to calculate the isentropic efficiency and volumetric efficiency at nominal frequency, respectively.

$$\eta_{\text{isen,nom}}=1.006-0.121\frac{P_1}{P_2} \tag{16}$$

$$\eta_{\mathrm{vol,nom}} = 1.079 - 0.1053\frac{P_1}{P_2} \tag{17}$$

where P_1 and P_2 are the discharge and suction pressures.

Equation 18 derived from the manufacturer data of a carbon dioxide compressor is implemented to calculate both the isentropic and volumetric efficiencies at any arbitrary frequency, f, between the range of 0 to 65 Hz.

$$\frac{\eta}{\eta_{\mathrm{nom}}} = 0.91 + 0.18 f_{\mathrm{r}} - 0.09 f_{\mathrm{r}}^2 \tag{18}$$

where f_{r} refers to the frequency ratio of f/f_{nom}.

The enthalpy of the CO_2 at the discharge (States 5 and 7), h_1, of the compressor is obtained using Eq. (19), and the power consumption is calculated by Eq. (20). The mass flow rate in the loop is calculated by Eq. (21).

$$h_1 = h_2 + \frac{h_{1\mathrm{s}} - h_2}{\eta_{\mathrm{isen}}} \tag{19}$$

$$W_{\mathrm{com}} = \dot{m}_{\mathrm{CO_2}}(h_1 - h_2) \tag{20}$$

$$\dot{m}_{\mathrm{CO_2}} = \eta_{\mathrm{vol}} \rho_{\mathrm{CO_2}} V_{\mathrm{rev}} f \tag{21}$$

Where $h_{1\mathrm{s}}$ is the isentropic enthalpy, h_2 is the suction enthalpy, ρ_{CO2} is the density at the suction of the compressor and V_{rev} is the displacement volume of the compressor.

3.4 Flash tank

In the present model, seeing in Fig. 1, the two-phase CO_2 (State 8) and superheated vapor CO_2 (State 5) enter the flash tank, and exit as saturated vapor CO_2 (State 6) from the top port of the flash tank. The following simplifications are adopted.

1) Two Phases separate perfectly inside the flash tank.
2) There is no pressure drop inside the flash tank.

3) The vapor and liquid in the flash tank are in thermodynamic equilibrium.

4) The energy balance in the flash tank can be expressed by the following equation.

$$\dot{m}_{CO_2,H}(h_1 - h_2) = \dot{m}_{CO_2,I}(h_6 - h_8) + \dot{m}_{CO_2,L}(h_5 - h_6) \tag{22}$$

3.5 Expansion valve

The expansion processes from State 1 to State 8 and from State 2 to State 3 are assumed that the enthalpy value before an expansion valve is equal to that after the expansion valve, i.e., h_1=h_8 and h_2=h_3.

3.6 Carbon dioxide hydrate decomposer and carbon dioxide evaporator

The CO_2 hydrates format in the tank reactor at temperature of 7 °C and circulates the hydrate slurry to melt at 7 °C as well. Thus, the low-stage pressure equals to the equilibrium pressure, 2.78 MPa, corresponding to the equilibrium temperature of 7 °C. The LMTD method is calculate the heat transfer area of the CO_2 hydrate decomposer and the CO_2 evaporator (finned-tube heat exchangers here as adopted). The overall heat transfer coefficient and the heat transfer area are calculated by Eqs. (23) and (24).

$$\frac{1}{U} = \frac{A_i}{h_a(i)A_o} + \frac{A_i \ln\left(d_o / d_i\right)}{2\pi k_{wall} l} + \frac{1}{h_{hyd/CO_2}} \tag{23}$$

$$A = \frac{Q}{U \times LMTD} \tag{24}$$

The evaporator of the SC-VCRS is divided into two parts, namely two-phase and single-phase. The air inlet and outlet temperatures are assumed as 23 °C and 18 °C with temperature difference of 5 °C. The orders of magnitude of the heat transfer coefficients for CO_2 evaporation and single-phase in tubes are obtained by of Hwang et al. [21] and Mac Adams [22] correlations. They are round 40000 W/m^2 k and 2000 W/m^2 k in the tubes with diameter of 10 mm. Those values are also recommended by Diaby et al. [36]. The value for air is of the order of magnitude of 100 W/m^2 k, which is obtained by the correlation of Wang et al. [23]. For the convective heat transfer coefficient of the CO_2 hydrate slurry in tubes, the research by Oignet et al. [28] suggested that the value can reach 3500 W/m^2 k for solid fraction of 14 vol.% with a Reynolds number around 2300.

3.7 Performance evaluation

As defined in Eq. (25), the COP of the system is the ratio of cooling capacity and total power consumption. The total power consumption comes from the compressors in the primary CO_2 loop, which is referred in Eq. (20), as well as the water pump and the air fan in the cooling tower loop. Relevant correlations can be found in Table 2.

$$COP = \frac{Q_{\mathrm{cooling}}}{W_{\mathrm{comp,H}} + W_{\mathrm{comp,L}} + W_{\mathrm{pump,ct}} + W_{\mathrm{fan,ct}}} \tag{25}$$

Table2 Details of power consumption correlations for cooling tower

Component	Correlation
Pump power [29]	$W_{\mathrm{pump}} = 3.57 m_{\mathrm{w}} H \rho_{\mathrm{w}} / \eta_{\mathrm{pump,ct}}$
Fan power [30]	$W_{\mathrm{fan}} = (1+u) \times 3600 m_{\mathrm{a}} / (10728 \rho_{\mathrm{mix}})$
Water make-up flow rate [29]	$m_{\mathrm{w,m\_up}} = EC/(C-1)$
Water blow-down flow rate [29]	$m_{\mathrm{w,b\_down}} = E/(C-1)$

u: water vapor to dry air ratio, ρ_{mix}: humidity air density, C: cycle of concentration

3.8 Economical model

Equation (26) is used to determine the total operating cost of design day. It mainly consists of two parts, namely the cost of the electricity consumption and the cost of the water make-up and blow-down. The latter part is produced from the water supplied to the cooling tower due to the reduction of evaporation loss and the daily maintain

$$C_{\mathrm{op}} = C_{\mathrm{op,E}} + C_{\mathrm{w,m\_up}} = \int_0^{t_{\mathrm{op}}} e_{\mathrm{tariff}} W dt + \int_0^{t_{\mathrm{op}}} w_{\mathrm{tariff}} V_{\mathrm{w}} dt \tag{26}$$

where e_{tariffs} and w_{tarffs} refer to the localized electricity (£ kWh^{-1}) and water (£ m^{-3}) tariff rates, respectively. V_{w} is the water volume cost. w_{tarffs} is estimated to 2 £/m^3.

Table 1 gives the water flow rates of make-up and blow-down for the cooling tower. Blow-down and make-up are as functions of evaporation loss, which can be calculated by Eq. (27).

$$E = 0.00546 m_{\mathrm{w,ct}} R \tag{27}$$

Where R refers to the range of cooling tower, *Rang:* $R = T_{\mathrm{w,su}} - T_{\mathrm{w,ex}}$.

The correlations listed in Table 3 are used to estimate the capital costs of the main components in the vapor-compression refrigeration systems.

Table 3 Details of capital cost correlations for main components

Component	Correlation
Compressor [31]	$C_{\mathrm{comp}} = 10167.5 {m_{\mathrm{CO_2}}}^{0.46}$
Gas cooler [31]	$C_{\mathrm{gc}} = 2382.9 {A_{\mathrm{gc}}}^{0.68}$
CO_2 hydrate decomposer and CO_2 evaporator [32]	$C_{\mathrm{dec/evap}} = 1397.9 {A_{\mathrm{dec/evap}}}^{0.89}$
Cooling tower [29]	$C_{\mathrm{ct}} = 148.05(13.11 m_{\mathrm{w}})^{0.79}(0.12R)^{0.57}(0.18A)^{-0.9924} + (0.022 T_{\mathrm{wb}} + 0.)^{2.441}$
Expansion valve [31]	$C_{\mathrm{eval}} = 114.5 m_{\mathrm{CO_2}}$
Flash tank [33]	$C_{\mathrm{flash-tank}} = 280.3 {m_{\mathrm{CO_2}}}^{0.67}$
Hydrate tank [34]	$C_{\mathrm{hyd-tank}} = 8.67 \times 10^{2.9211 \exp(0.1416 \log V_{\mathrm{tank}})}$

Rang: $R = T_{\mathrm{w,su}} - T_{\mathrm{w,ex}}$, *Approach*: $A = T_{\mathrm{w,ex}} - T_{\mathrm{air,wb,su}}$

In addition, Equation (28) is used to calculate the total annual cost, including three parts: the annual repayment of initial capital investment, the total annual operation cost and the annual salvage value.

$$C_{\mathrm{tot}} = CRF \times C_{\mathrm{cap}} + C_{\mathrm{op}} - SV\left(\frac{i}{(1+\mathrm{i})^{n} - 1}\right) \tag{28}$$

The capital recovery factor (CRF) in Eq. (29) is defined as the ratio of a constant annuity to the present value of receiving that annuity for a given length of lifetime [35].

$$CRF = \frac{i(1+\mathrm{i})^{n}}{(1+\mathrm{i})^{n} - 1} \tag{29}$$

Where i refers to the annual interest and n is the years of the system lifetime. Salvage value, SV, the estimated value that an asset will realize upon its sale at the end of its useful life (is given in Table 4 as a percentage of the initial capital cost).

Table 4 Parameters of economic analysis

Parameter	Value
Annual interest rate (%)	14
Salvage value rate (%)	10

3.9 Modelling procedure

The flowchart of modeling of the CHB-VCRS is showed in Fig. 3. The procedures of detailly iterating the frequencies of the compressors at low-pressure stage, f_{L}, and high-pressure stage, f_{H}, are presented in Fig. 4, respectively. The residual values of ε (in Figs. 3, A2, B1 and B2) are adopted very carefully to ensure an appropriate computation cost and a deviation between Q_{target} and $Q_{\mathrm{calculate}}$ within ±0.5%. The codes are written in FORTRAN. The thermodynamic and transport properties of the working fluids are calculated by REFPROP 9.0.

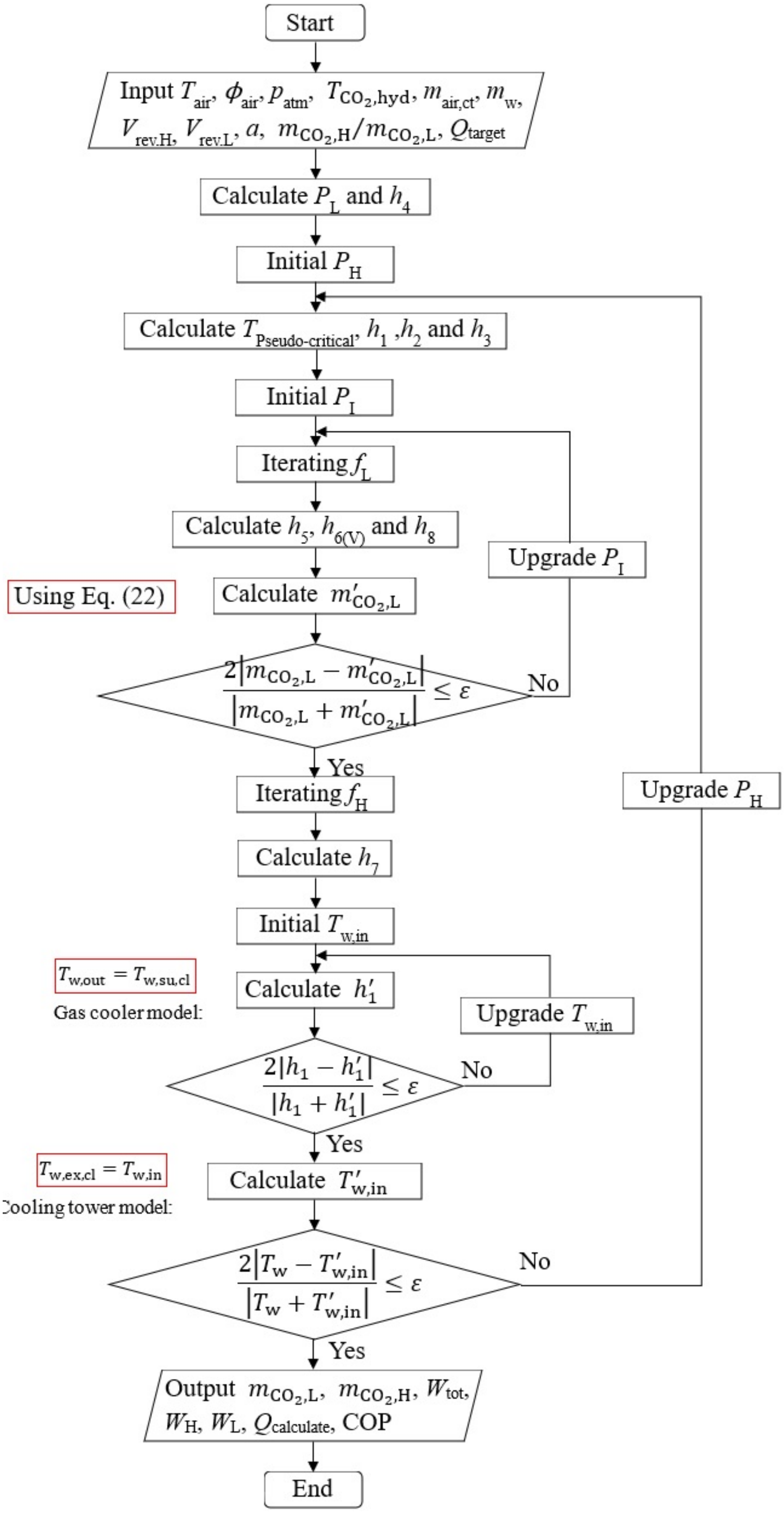

Figure 3 Flowchart of modelling of CHB-VCRS

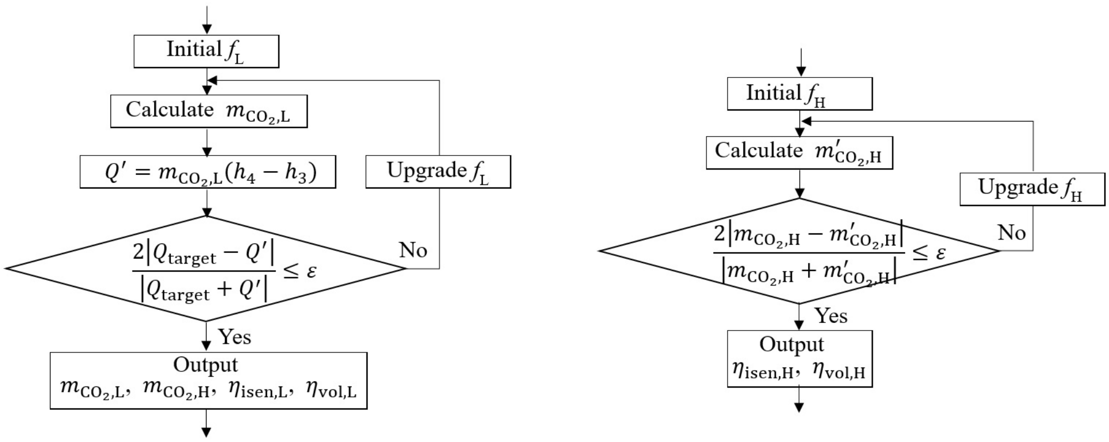

Figure 4 Flowchart of iterating f_L and f_H

4. Design parameters and controls for simulation

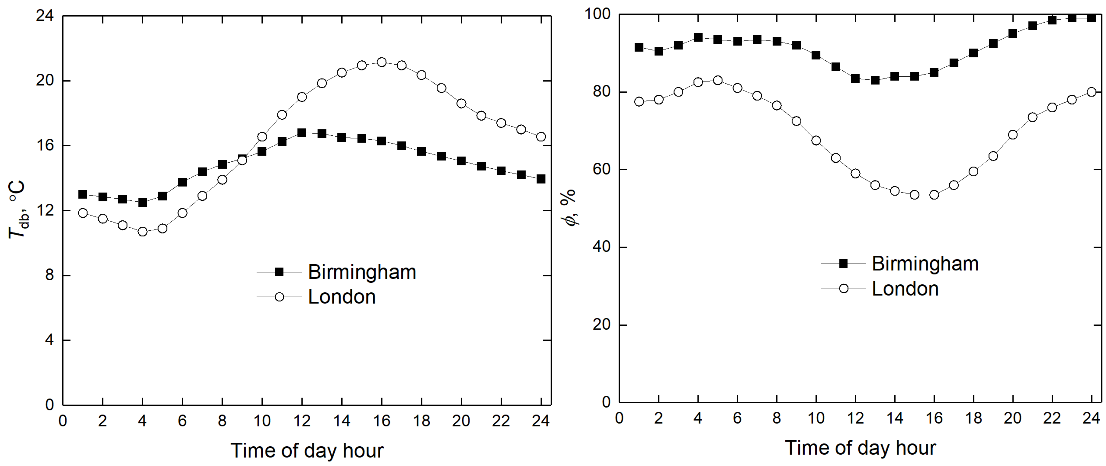

(a) (b)

Figure 5 Hourly dry temperature and relative humidity of design day in Birmingham and London

The ambient dry-bulb temperature and relative humidity records for Birmingham and London in the United Kingdom on the design day of 31 July are as shown in Fig. 5, which is used as the typical ambient conditions for the simulation. It illustrates that London had higher dry-bulb temperature, lower humidity as well as more remarkable their diurnal change due to the urban hot island effect [36], though both cities have a marine west coast climate. The weather data in the figure is sourced from Typical Meteorological Year 2 (TMY2) files in TRNSYS 17 libraries [37].

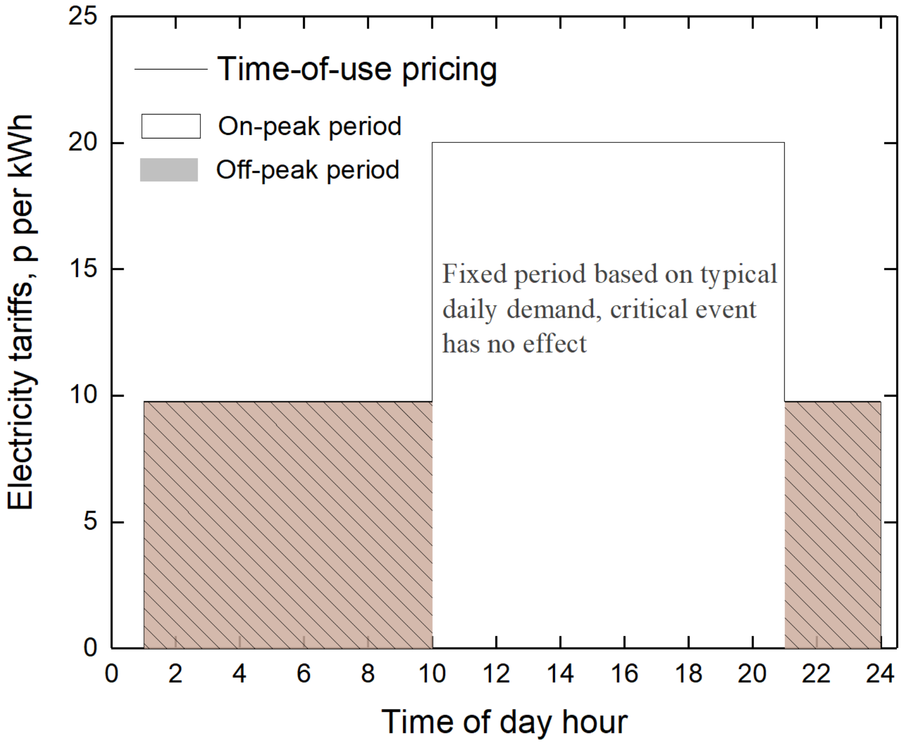

Figure 6 Time-variant pricing of design day

Time-of-use pricing of the electricity in Fig. 6 is used for the estimation of the operating cost. The electricity utilities often construct their tariffs around on-peak and off-peak schedules, which have strong incentives for the customer to shift the cooling load from on-peak to off-peak. Economy 7 and Economy 10 are two energy price plans suggested by the UKPower [38] to the customers who prefer a 'time of use' tariff. These two plans mean charge a cheaper rate for seven and ten nighttime hours than during the rest of the day. The off-peak hours are most likely being consecutive period between 22:30 and 8:30. For the simplification, two periods, i.e., 12 on-peak hours (10:00 to 22:00) and 12 off-peak hours (22:00 to 10:00), are created in this work. The average price of electricity during on- and off-peak are 20.03 and 9.76 pence per kilowatt-hour (with ratio of 2.1) for the standard rate (between April 2019-April 2020), respectively. These data is sourced from the English Housing Survey [39]. In addition, the economic parameters affected by the electricity prices ratio of on- and off-peak (range from 1.0 to 8.0) will be discussed in the following sections.

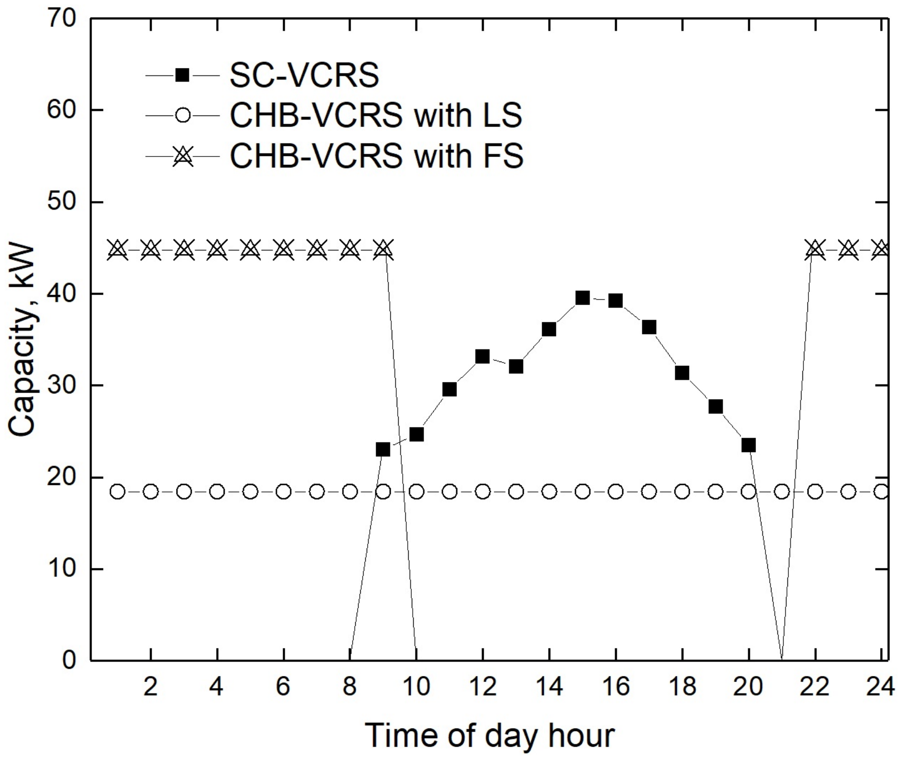

Figure 7 Capacities of SC-VCRS, CHB-VCRS with LS and CHB-VCRS with FS

The cooling load profile (solid-square) in Fig. 7 is calculated by TRNSYS 17. It is modeled under Birmingham weather conditions during 24 hours of a typical summer day in a typical meteorological year. The reference building of SFH 45 recommended by the IEA standard [40] is selected. It is assumed to be occupied from 9:00 to 20:00 in a 12-hour cooling of design days. The design room temperature is 20 °C and other input data can be found in Table 5. This building has a peak load of 39.54 kW at 15:00 with a total cooling requirement of 376.3 kWh. Moreover, a total of 150 days during the whole summer (5 days×4 weeks×6 months+30 days) is selected, considering the heating season in Birmingham from 1st October to 30th April. Extra 30 days are design margin.

Table 5 Input data of building cooling load calculation

Component	Description/value
Design room temperature (°C)	20.00
Building type	SFH 45 [40]
Building gross area (m^2)	1440
Working hours	9:00 to 20:00
Average occupant number per hour (person)	8
Average electrical gain per hour (W)	580
Annual working days (day)	150
Derating factor	0.70

The load profile in the figure defines the real-time cooling capacity for the non-storage single-stage CO_2 vapor-compression refrigeration system (SC-VCRS), which is descripted in Fig. 8. Therefore, the design capacity of the SC-VCRS equals the peak load. It means that the compressor is only running at the nominal frequency when full capacity of 39.54 kW cooling is required. The compressor runs in variant-speed to meet the cooling load during the rest time. Notice that, different from the two-stage system in Fig. 1, there is no split of the CO_2 flow at the exit of the gas-cooler for the SC-VCRS. The supercritical CO_2 with high pressure and high temperature (State 5 in Fig. 8) discharged from the compressor would be cooled to reach State 2 directly. There is no flash tank, and the subcooling (from State 1 to State 2) is operated in the gas-cooler. Then experiencing an expansion process, the two-phase CO_2 with low pressure and low temperature (State 3) is delivered into the evaporator. Finally, the superheated vapor

CO_2 (State 4) flows back to the compressor. The flowchart of modeling of the variant-speed SC-VCRS can be found in Fig. (C1)

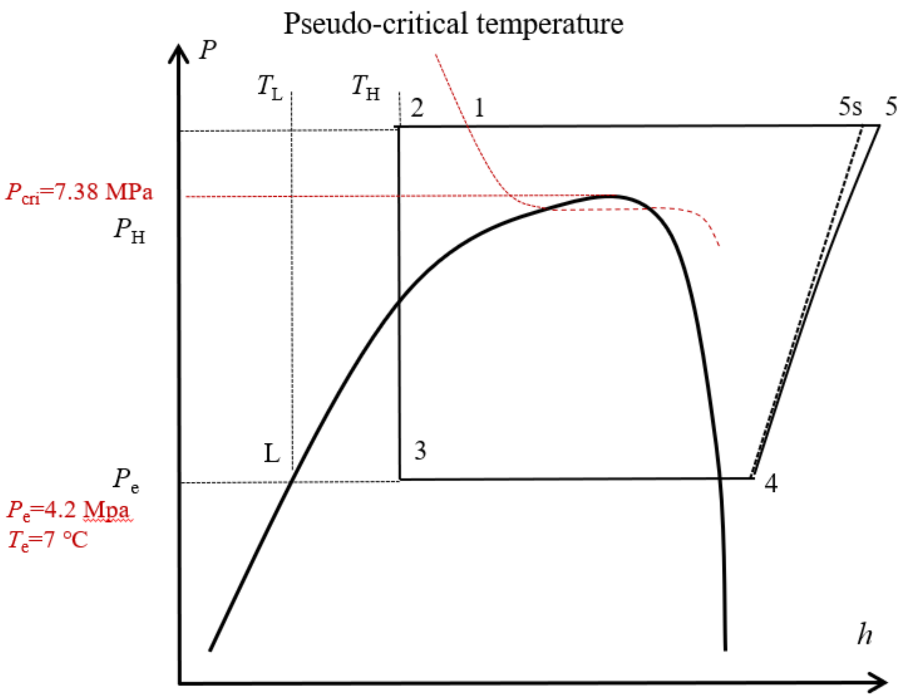

Figure 8 P-h diagram of SC-VCRS (baseline)

The procedure for the SC-VCRS is not the case when designing the size of a VCRS with CTES, the design capacity of which must be able to meet the total cooling load over the working-hour period. Therefore, it is significant to accurately calculate the total integrated load. A derating factor is introduced to estimate the efficiency losses in CTES charge-discharge cycles at nigh time. Generally, this factor is related to the standards of the ice-storage tank from the manufacturer. In this work, the value of the derating factor is estimated at 0.70, which is recommended by Silvertti [41] in design of an ice slurry based CTES. This factor typically varies between 0.65 and 0.70. Based on the discussion above, the design capacity of a VCRS with CTES can be calculated using the following equation:

$$Capacity\ \mathrm{kW} = \frac{total\ \mathrm{kWh}}{day\ hours + derating\ factor \times nighty\ hours} \tag{30}$$

Load-leveling storage and full storage strategies are implemented for the CHB-VCRS, and compared with the non-storage SC-VCRS (as baseline). As presented in Fig. 7, the CHB-VCRS with LS evenly transfers the entire on-peak cooling load to the whole design day, which means the system works at constant capacity throughout 24 hours. During the on-peak period, when the cooling load is less than the design capacity, the excess coolth energy is stored. Conversely, when the load exceeds the capacity, the additional demand is discharged from the storage. For the CHB-VCRS with FS, the system operates on its full capacity from 22:00 to 10:00 (12 hours), which transfers the entire on-peak cooling load to the off-peak period. The design capacities of CHB-VCRS under LS and FS strategies calculated by Eq. (30), are 17.84 kW and 43.33 kW, respectively. The FS system does not run during on-peak time, therefore it requires relatively large refrigeration and storage capacities. As listed in Table 6, the capacity of the CHB-VCRS with LS is just 45% of the SC-VCRS while the capacity of the FS system is 10% higher than the baseline.

Table 6 Summary of capacity calculation

Description	Capacity (kW)	Comparison
SC-VCRS	39.54	100%
CHB-VCRS with LS	17.84	45%
CHB-VCRS with FS	43.33	110%

A series of trial-runs are implemented to figure out the configurations of the main components, including the gas cooler, the compressor and the cooling tower. The basic configurations are firstly determined, when the system operates in full design capacity (compressors run at nominal frequency). The maximum pressure at high stage of design day is obtained. For a normal VCRS, higher high-stage pressure results in a loss of COP. In order to maintain the CO_2 systems always running in the trans-critical region and a relatively high overall COP of whole design day, further refining and finalizing of the configurations is implemented. The iterative steps are to ensure the high-stage pressure be located as close as possible to the critical pressure (7.38 MPa), when the system operates under the conditions of the lowest dry-bulb temperature and lowest relative humidity. At this point, it reaches the minimum pressure at high stage of system of design day. Table 7 lists the final configurations and the other important system parameters.

Table 7 Specification of system component design parameters and controls

Component	Parameter	Value
CHB-VCRS		
CO_2 hydration and dissociation	Equilibrium temperature (°C)	7.0
Gas cooler (LS)	Heat transfer area (m^2)	0.43
Gas cooler (FS)	Heat transfer area (m^2)	1.39
Mass flow rate ratio	$m_{CO_2,H}/m_{CO_2,L}$	3
Compressor (LS)	Displacement volume -H (cm^3 rev^{-1})	27
	Displacement volume -L (cm^3 rev^{-1})	38
Compressor (FS)	Displacement volume -H (cm^3 rev^{-1})	66
	Displacement volume -L (cm^3 rev^{-1})	93
Cooling tower (LS)	Air supply mass flow rate (kg s^{-1})	2.80
	Water supply mass flow rate (kg s^{-1})	0.47
Cooling tower (FS)	Air supply mass flow rate (kg s^{-1})	3.24
	Water supply mass flow rate (kg s^{-1})	1.15
SC-VCRS		
Evaporator	Evaporating temperature (°C)	7.0
Gas cooler	Heat transfer area (m^2)	0.14
Compressor	Displacement volume (cm^3 rev^{-1})	42

Cooling tower	Air supply mass flow rate (kg s^{-1})	3.25
	Water supply mass flow rate (kg s^{-1})	1.45
Common design		
Gas cooler	Inner diameter of inner tube (m)	0.012
	Outer diameter of inner tube (m)	0.018
	Inner diameter of outer tube (m)	0.027
	Fictitious subcooling degree (-)	0.5
Dissociation reactor/evaporator	Outer diameter (m)	0.00952
	Inner diameter (m)	0.0082
	Tube pitch (m)	0.0254
	Fin pitch (m)	0.002
Compressor	Superheating (°C)	15.0
Cooling tower	Range/$T_{w,su}$-$T_{w,ex}$ (°C)	10.0
	Cycle of concentration	4
	Water pump efficiency	0.6

5. Comparison of coefficient of performance, power consumption and operating cost

Figures 9 demonstrate the hourly variations of the COP. In general, the COP of the SC-VCRS is higher than those of both the HBC-VCRSs. There are three reasons. One is the higher low-stage pressure of the SC-VCRS, 4.18 MPa, corresponding to 7 °C evaporation temperature. Whereas the low-stage pressure of the CHB-VCRSs is only 2.78 MPa, corresponding to 7 °C equilibrium temperature. The other is the variable-speed compressor for the SC-VCRS. It can maintain the high-stage pressure of the SC-VCRS operating at a relative low-level, especially at worst weather conditions and when the hourly cooling load has great fluctuation. The last and most important is the different characteristics between single-stage and two-stage thermodynamic cycles. Compared to the single-stage system for the COP formula for the two-stage system (seeing Eq. (5)), the enthalpy difference of the second term on the denominator needs to be multiplied by the mass flow ratio of high- and low-stages, r (with the value of 3.0 in present simulation), which significantly decrease the COP.

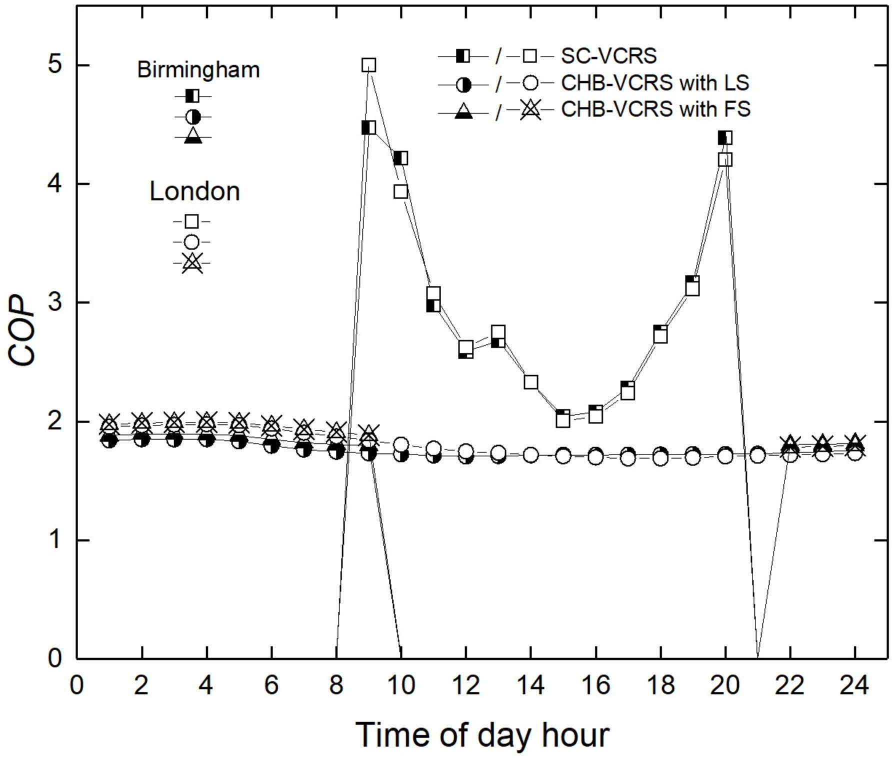

Figure 9 Time-variant COP of design day

In addition, the COP of the CHB-VCRS with LS has non-obvious improvement at nighttime, only 8-17% and 5-12% for Birmingham and London, respectively, as it is only slightly affected by ambient temperature and humidity. The system is operating with constant capacity in all working hours, thus the COP mainly depends on the compressor power consumption. Therefore, the compression ratio and the mass flow rate are considerable factors. The temperature of the cooling water supplied to the gas cooler strongly affects the high-stage pressure. In the present case, the dry-bulb temperature at nighttime is lower than that at daytime, which improves the performance of the cooling tower, however, the relative humidity increases at nighttime which depresses the cooling tower. Based on this, the cooling water temperature is relative stable, as a result that the high-stage pressure changes very slightly. Coupled with the almost unchanged mass flow rates ratio of the high- and low-stages, the compression ratio and the mass flow rate hence fluctuate moderately. The hourly variations of the frequencies of the high- and low-stage compressors for the CHB-VCRS can be found in Fig. 10. They are slightly changed from 58 Hz to 61 Hz. All of these led to the COP fluctuation of CHB-VCRS smoothly and slightly. The overall COP of the FS system is a litter higher than that of the LS system, because of the diminution part, i.e., daytime COP, influencing the overall performance for the latter system. On the contrary, the COP of the SC-VCRS changes dramatically. The mass flow rate of CO_2 in the gas cooler has strong influence. The SC-VCRS raises or reduces the compressor frequency to adjust the mass flow rate to meet the higher or lower cooling requirements all day. As depicted in Fig. 10, the frequency of the SC-VCRS obviously varies from 33 Hz to 60 Hz. When the notably reduced mass flow rate of supercritical CO_2 passes through the gas cooler, the high-stage pressure has to decrease to balance the heat transfer between the CO_2 and the water sides. Consequently, the COP rises significantly. Conversely, the COP drops sharply.

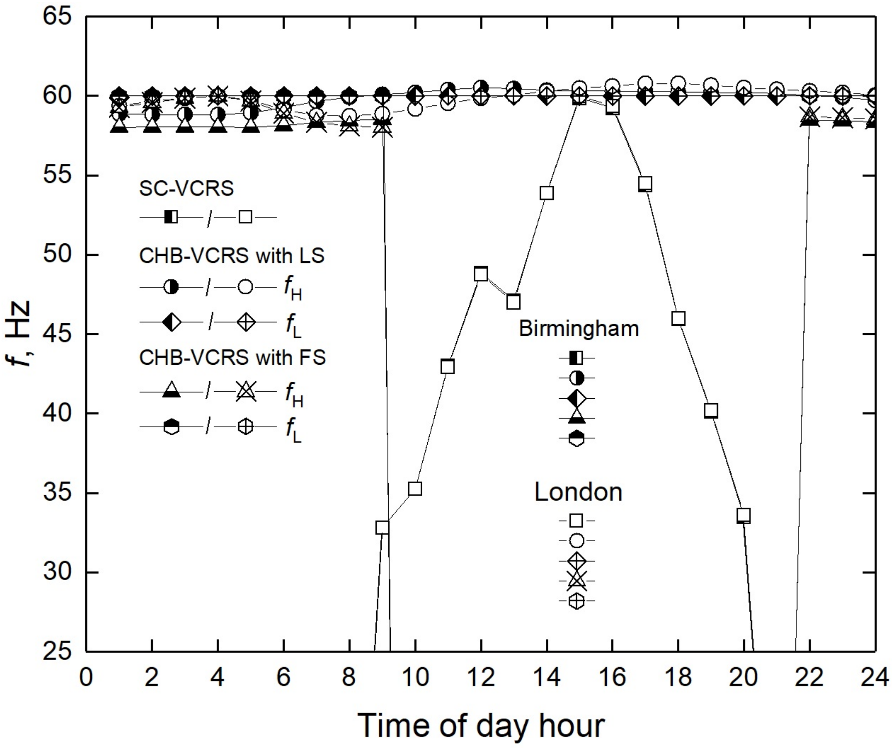

Figure 10 Time-variant compressor frequency of design day

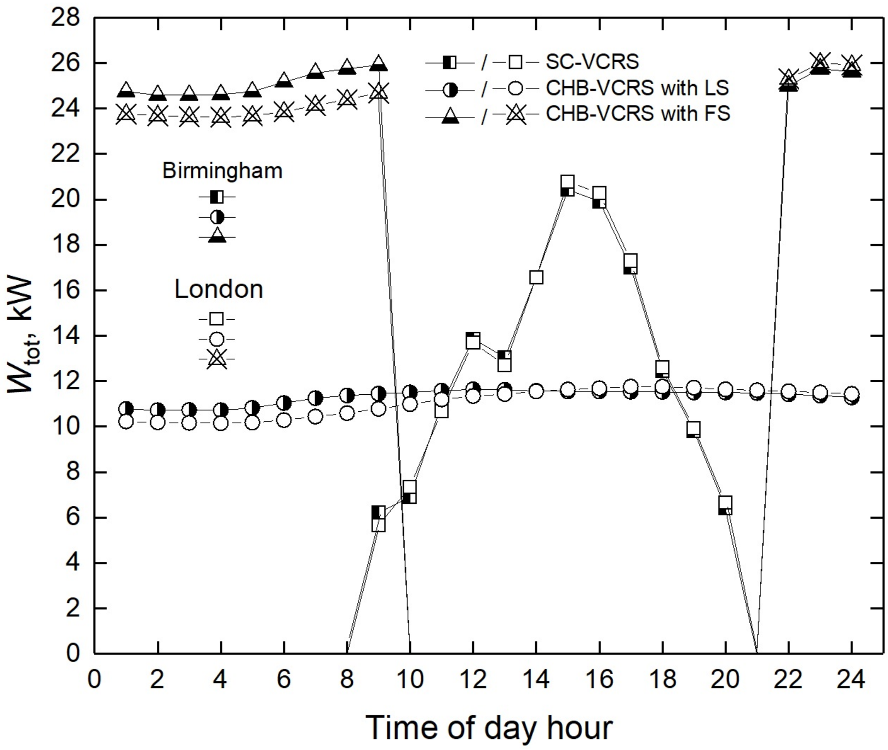

Figure 11 Time-variant total power consumption of design day

Figures 11 present the hourly variations of the total power consumption. It has the similar tendency with the frequencies in Fig. 10. As seen in Fig. 11, the total power consumption mainly comes from the compressors, which depends on the compression ratio and the mass flow rate. Because of the largest cooling capacity, the CHB-VCRS with FS has the highest hourly power consumption. The detailed distributions of the power consumption are presented in Fig. 12. As depicted, the CHB-VCRS with FS has the maximum total power consumption of design day, but the lowest ratio of the part from cooling tower occupied. The non-storage system has the smallest total power consumption, but the largest percentage consumed by the cooling tower. More details can be found in Table 8. Additionally, the FS system consumes the lowest power of cooling tower and the LS system expends the highest.

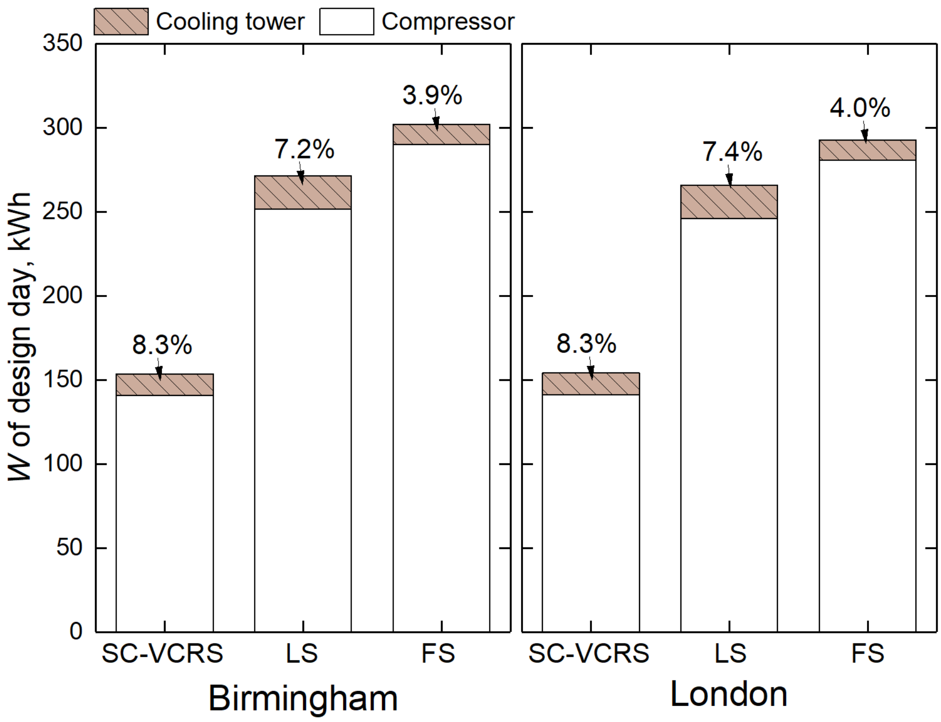

Figure 12 Details of total power consumption of design day

Table 8 Details of COP, power consumption and operating cost of design day

	$COP_{overall}$	W_{comp} (kWh)	W_{ct} (kWh)	$C_{op,E}$ (£)	C_{w,m_up} (£)	C_{op} (£)
Birmingham						
SC-VCRS	2.67	140.83	12.78	30.13	1.67	31.80
CHB-VCRS with LS	1.78	251.85	19.69	40.74	0.58	41.32
CHB-VCRS with FS	1.85	290.30	11.81	29.50	1.40	30.90
London						
SC-VCRS	2.66	141.47	12.78	30.31	1.67	31.98
CHB-VCRS with LS	1.80	246.12	19.69	40.14	0.58	40.72
CHB-VCRS with FS	1.92	280.96	11.81	28.59	1.40	29.99

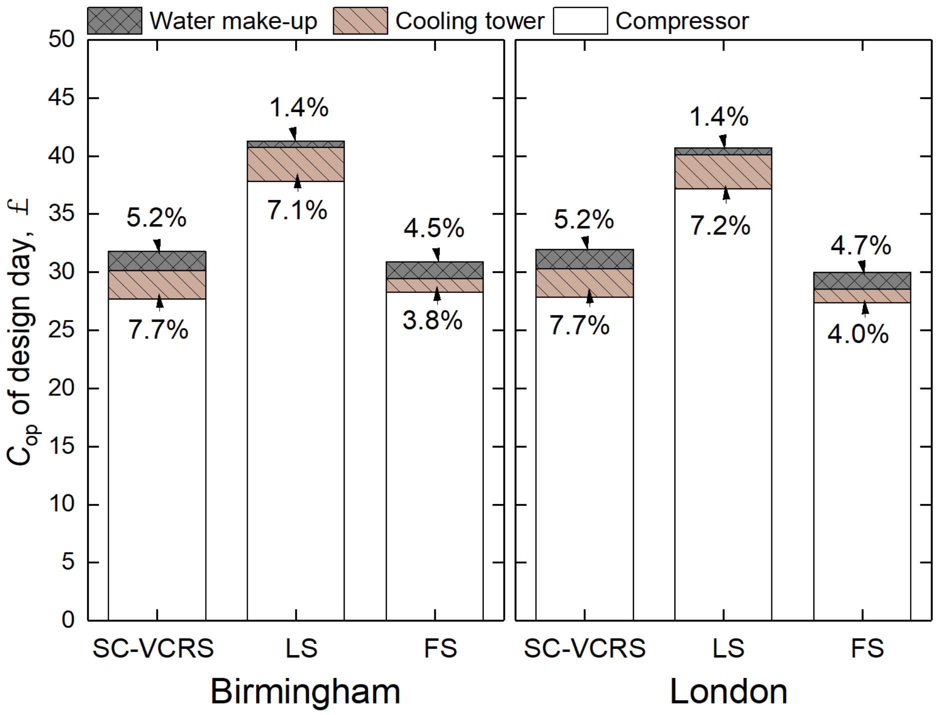

Figure 13 Details of total operating cost of design day

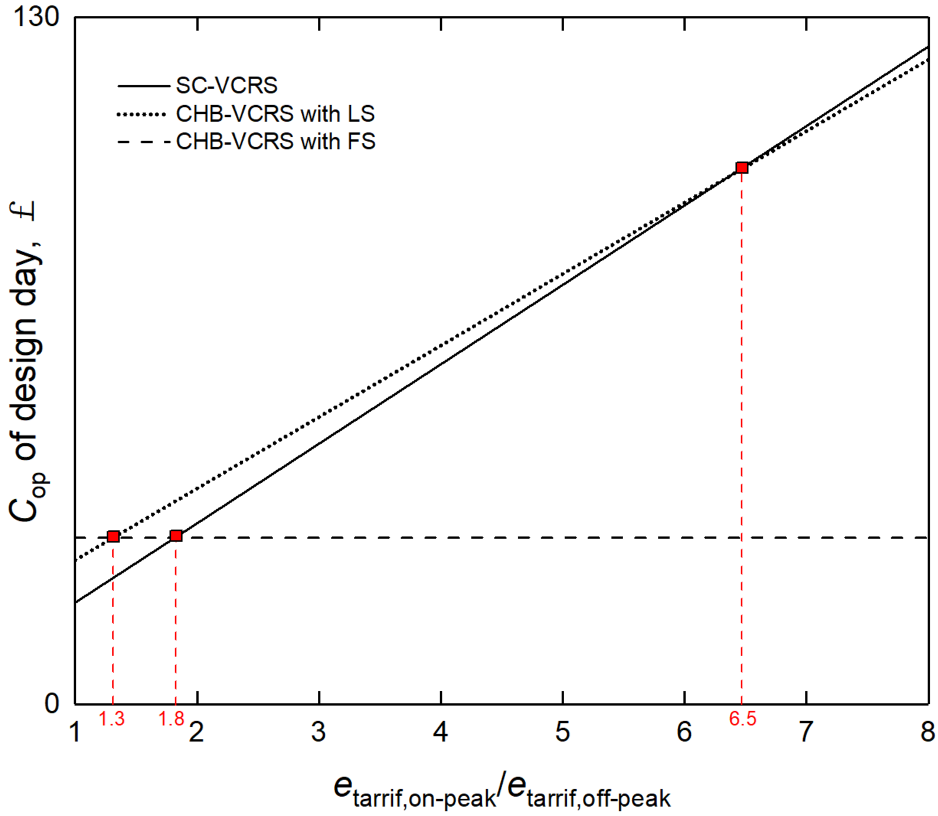

Figure 14 Total operating cost variation with the electricity prices ratio

Figure 13 presents the detailed distribution of the daily operation cost. In general, the CBH-VCRS with FS has the lowest total operating cost, which is 26.4% and 6.3% lower than those of the LS system and the SC-VCRS, respectively. Major operating cost comes from the compressors, almost 90% of total. The operating cost of the cooling tower includes the electricity and water consumption. The former is higher and occupies no more than 7.7%. The SC-VCRS consumes the maximum amount of the water every day, and the LS system has the most saving on it. More details are listed in Table 8.

Figure 14 described that the daily operation cost varies with the increasing of the electricity prices ratio of on- and off-peaks. Because of the system only operates during off-peak period, C_{op} of the CHB-VCRS with FS maintains unchanged. C_{op} of the SV-VCRS and the CHB-VCRS with LS raise notably. The first two intersections are that the C_{op} of the SV-VCRS and the LS system across C_{op} of the CHB-VCRS with FS at the price ratios of 1.3 and 1.8, respectively. The third one means that the C_{op} of the SV-VCRS exceeds that of the LS system at the price ratios of 6.5.

6. Comparison of initial capital cost and total annual cost

The initial capital cost and its influence on the total annual cost and the payback period of additional expense under different electricity tariffs structures are carried out in this section.

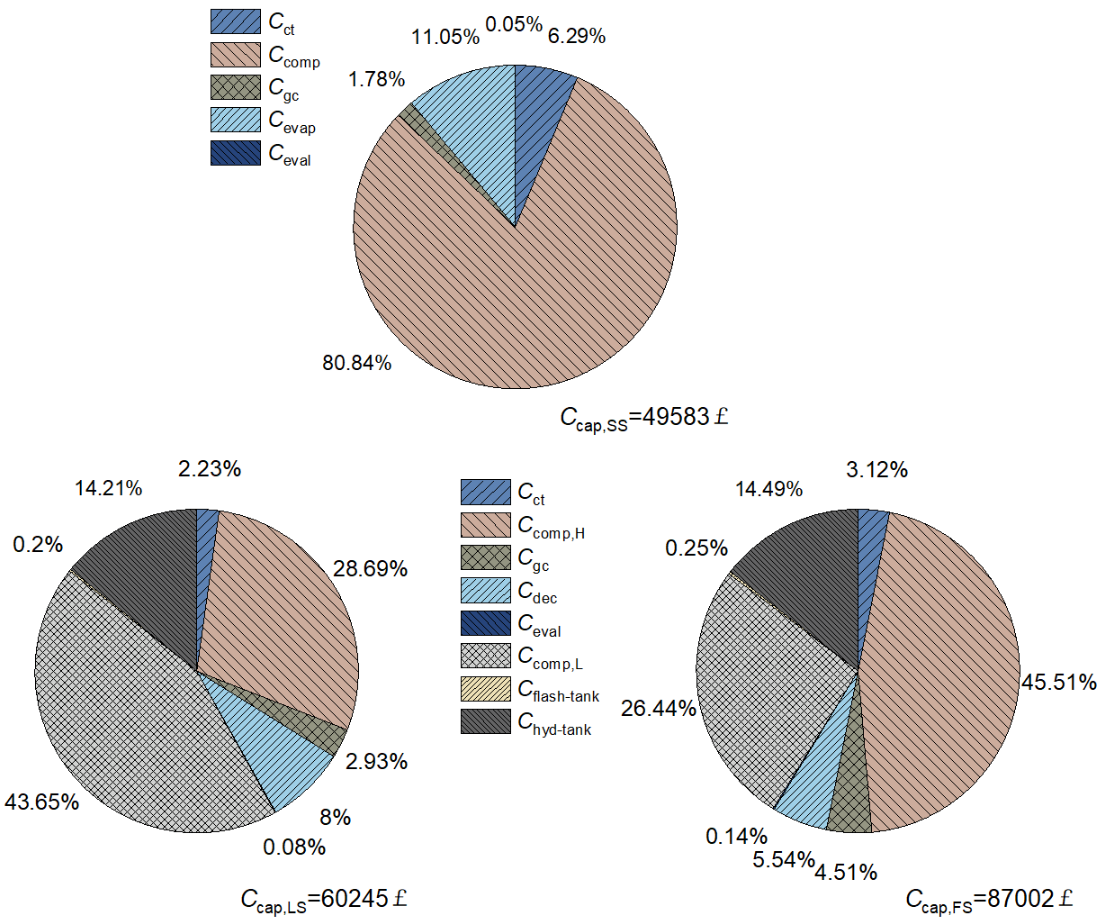

Figure 15 Details of initial capital cost for three systems

Figure 15 gives the detailed distribution of the main components cost. Because of the largest design capacity, the CHB-VCRS with FS pays the highest initial capital cost, which is 44.4% and 75.5% higher than those of the CHB-VCRS with LS and the SC-VCRS. The compressor is absolutely the major cost. This part accounts for 80.8%, 72.3% and 72.0% of the total costs for the conventional, LS and FS systems, respectively. For the CHB-VCRS, the hydration tank is the second major cost, which comprises 14.2% and 14.5% for the LS and FS systems, respectively. For the non-storage SC-VCRS, the second costly equipment is evaporator, which is around 10.8% of total. The hydrate decomposer of the LS and FS systems only make a spend of about 8.0% and 5.6%. The gas cooler and cooling tower for the three systems occupy the costs of the total in the range of 1.6-6.3%. The rest components, such as the expansion valve and flash tank, expends less than 1% of the total. Based on these, it can be found that the cost of the CO_2 compressor shows the greatest impact on the total initial capital cost, which thus has the greatest potential to cut down the investment.

As well known, initial capital cost control is a basic design principle in engineering. This method has great potential particularly with the development of new materials and the globalization of industry. Therefore, the economic feasibility of the CHB-VCRS proposed in this work will be discussed in comparison of the annual costs that replacing the conventional SC-VCRS considering the improvement of the initial capital cost considering the variation of initial capital cost.

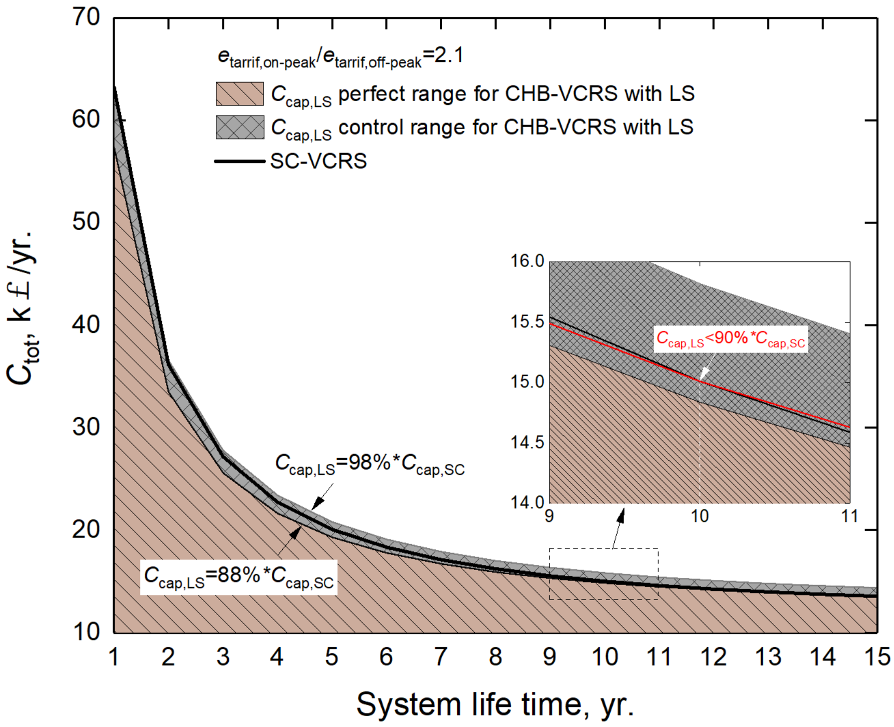

(a) Total annual cost as a function of system lifetime

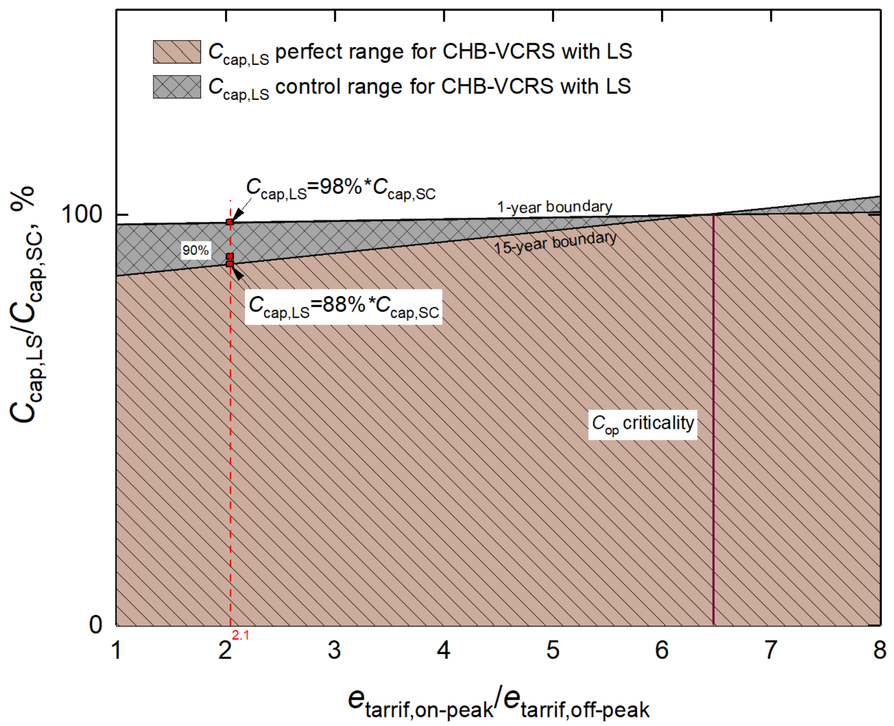

(b) As a function of electricity prices ratio of on- and off-peaks

Figure 16 Initial capital cost control for CHB-VCRS with LS

Figures 16(a) and 16(b) illustrate the indication range of the initial capital cost for the CHB-VCRS with LS that is worthy of replacing the SC-VCRS when the lifetime is set within 15 years. Generally, the total annual cost decreases with the increasing of the system lifetime. The electricity price ratio of on- and off-peak is adopted as 2.1 in Fig 16(a). The light-shadow area in the figure is called $C_{cap,LS}$ perfect range, which indicates the LS system can absolutely replace the base line when its initial capital cost is less than 88% of $C_{cap,SC}$. The white area that the $C_{cap,LS}$ larger than 98% of $C_{cap,SC}$ means there is totally no worthy replacement. For the dark-shadow area between 88% and 98% of $C_{cap,SC}$, the lifetime of the CHB-VCRS with LS need be calculated carefully for replacing the baseline. Taking the case in the enlarged area (enclosed by dotted line), the red line of 90% is the limitation for the LS system with the 10-year system lifetime. In fact, the control range of the initial capital cost for the LS system is quite narrow and the ceiling cannot beyond 100% when the electricity prices ratio set as 2.1, due to no advantage on the operation cost (as depicted in Fig. 14).

Fig 16(b) investigate the economic feasibility of the CHB-VCRS with LS affected by the increasing of the electricity prices ratio. The ceiling and floor line of the control area intersect at the point of (6.5, 100%). Comparing Fig. 14, the operation costs of the CHB-VCRS with LS and the SC-VCRS reach identical at the price ratio of 6.5. The corresponding vertical C_{op} criticality line (brown solid) divides the map into two zones. On the left hand side, it is the $C_{op,LS}$ advantage zone. Whereas on the right hand side, it is the $C_{op,LS}$ disadvantage zone. The control range become more and more narrow when the price ratio approaches to C_{op} criticality line. 1-year boundary and 15-year boundary switch their characteristics if crossing the zones. Generally, in the $C_{op,LS}$ disadvantage zone, the LS system should reduce their initial capital cost lower than 100% of baseline, that the CHB-VCRS would have the feasibility of replacing the SC-VCRS. However, in the $C_{op,LS}$ advantage zone, the CHB-VCRS start to have the flexibility on the initial capital cost. In this case, because of no advantage on the operating cost, the LS system nearly have no any flexibility, only 104.5% of $C_{cap,SC}$ even when the electricity ratio is 8.0. At last, noticed that the red dash line in Fig 16(b) points out the positions of those key boundary lines which exist in Fig. 16(a).

Figures 17(a) and 17(b) has the identical function as Figs. 16(a) and 16(b). These two maps are then used to assess the economic feasibility for the CHB-VCRS with FS. The electricity prices ratio in Fig17(a) is 4.0. The control range of 109-160% for the FS system is wider than that for the LS system. Different from the LS system, seeing Fig. 14, the FS system has superior advantage over the SC-VCRS on the operation cost. Thus the $C_{op,FS}$ advantage zone is huge and overwhelms the $C_{op,FS}$ disadvantage zone in Fig. 17(b). As viewed, the FS system has more flexibility, even the $C_{cap,FS}$ is over 250% of $C_{cap,SC}$ when the electricity prices ratio set as 8.0, A specific system lifetime (within 15 years) can be found, which means the FS system is worthy of replacing the SC-VCRS.

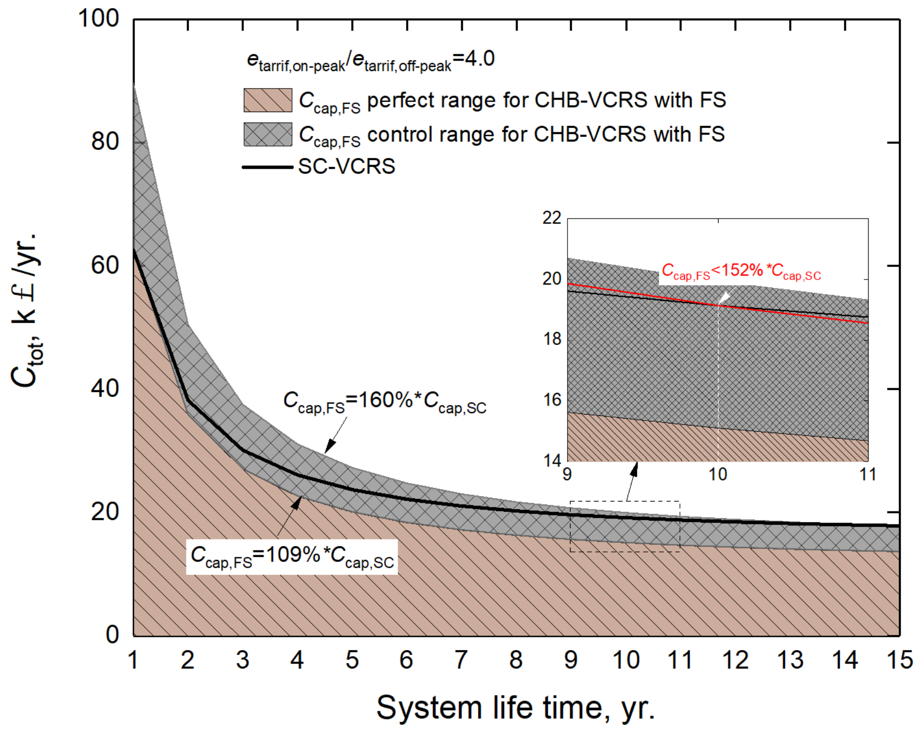

(a) Total annual cost as a function of system lifetime

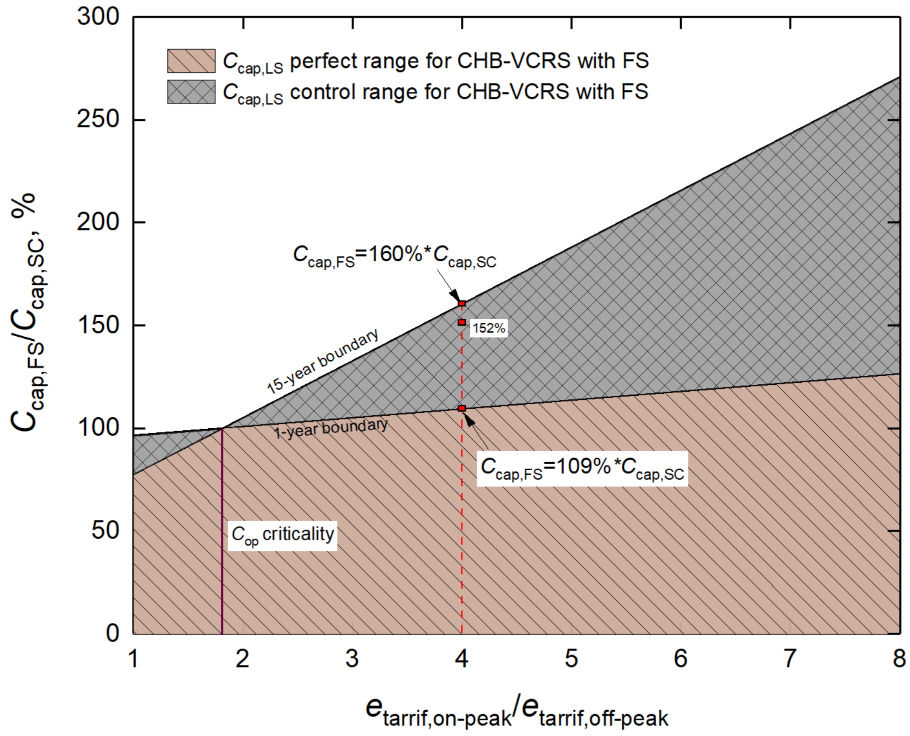

(b) As a function of electricity prices ratio of on- and off-peak

Figure 17 Initial capital cost control for CHB-VCRS with FS

The payback years of additional expenses when a system with larger operation cost but lower initial capital cost is replaced by a specific system with lower operation cost, but larger initial capital cost can be calculated iteratively by the following equation:

$$C_{\mathrm{op,diff}}\left(\frac{i(1+\mathrm{i})^{n}-1}{i(1+\mathrm{i})^{n}}\right)+SV\left(\frac{1}{(1+\mathrm{i})^{n}}\right)=C_{\mathrm{cap,diff}} \tag{31}$$

In Eq. (31), n refers to the payback years. $C_{\mathrm{op,diff}}$ is defined as the value of savings in the annual operating cost (e.g., based on Fig. 18, the difference in annual operating costs of the SC-VCRS and the CHB-VCRS with FS), and $C_{\mathrm{cap,diff}}$ is considered as the difference between the initial capital costs of the two systems. SV in Eq. (31) is assumed as 10% of $C_{\mathrm{cap,diff}}$.

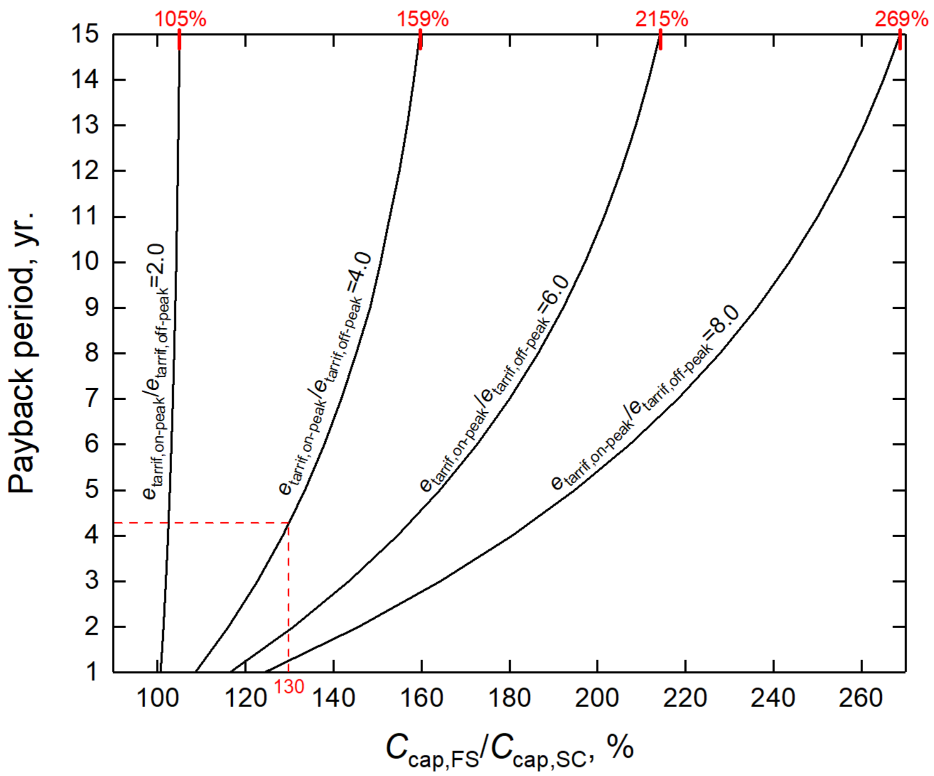

Figure 18 Payback period for extra capital cost in case of replacing SC-VCRS with CHB-VCRS with FS in a system lifetime of 15 years

As aforementioned, the burden on the operation cost of the SC-VCRS over that of the CHB-VCRS with FS is enlarged significantly with the increasing of the electricity prices ratio. This will strongly influence on the payback years of the additional expenses on the initial capital investment. As depicted in Fig. 18, the system lifetime of 15 years is pre-set, lower the burden results in the slop of the curve become steeper, which means the growth of the flexibility on the initial capital cost for the FS system would be smaller when the payback years is planned from 1 to the maximum value of 15. For instance, the growth of the flexibility would decrease from 51.0% of $C_{cap,SC}$ (109-159%) to 4.3% of $C_{cap,SC}$ (101-105%), if the electricity prices ratio increases from 4.0 to 2.0. In addition, Figure18 can be used as an indication map to estimate the profit years in case of the SC−VCRS replaced by the CHB-VCRS with LS in the lifetime of 15 years. Taking the electricity prices ratio of 4.0 as the example: If $C_{cap,FC}$ is larger than 159% of $C_{cap,SC}$, replacing with the FS system that the system cannot complete the payback for the extra expanses on the initial capital cost within 15 years; If $C_{cap,FC}$ is smaller than 105% of $C_{cap,SC}$, the FS system can accomplish the payback and make the profits since the first operation year; If $C_{cap,FC}$ is 130.0% of $C_{cap,SC}$, a value between 105-159%, it can be figured out (red-dash lines) in Fig. 18 that the FS system can pay off the extra expenses and start to earn the profits in the fifth year.

7. Conclusions

This paper proposed a new two-stage CHB-VCRS, which arranged formation and dissociation at the low-pressure stage andused pure CO_2 hydrates as the primary refrigerant. Detailed mathematic models were developed. The numerical simulations of the proposed CHB-VCRS applying two CETS operation strategies, i.e., load-levelling storage and full storage, were conducted under continuous 24 hours of design day in the summer of Birmingham and London. In addition, a conventional non-storage SC-VCRS was modelled as the baseline, which was used to make performance comparison based on thermo-economic analyses. The following conclusions are achieved:

(1) For two-stage CHB-VCRS, when the high- and low-stage pressures were fixed, there existed an optimum inter-stage pressure on the basis of maximum COP. This value increased with the increasing of the subcooling parameter.

(2) The design cooling capacity of the CHB-VCRS with LS was around 40% lower than that of the non-storage SC-VCRS. The design capacity of the CHB-VCRS with FS have the largest one, 10% larger than that of the baseline.

(3) In general, the CHB-VCRS with FS had the lowest annual operation cost, and with the incentivization of electricity-price ratio (from 2 to 8), this savings was significantly enlarged.

(4) The CHB-VCRS with LS saved most on the water consumption, whereas the non-storage SC-VCRS consumed most.

(5) The initial capital cost of the CHB-VCRS with FS was 71.1% and 44.4% higher than those of the SC-VCRS and the CHB-VCRS with LS, respectively. The compressor was the major cost for all the three systems.

(6) Compared to the FS operation, the CHB-VCRS using LS strategy had wider economic feasibility in replacing of the conventional SC-VCRS, because of the advantage on the annual operation cost. With higher electricity-price ratio, the LS system had more flexibility on the initial capital cost.

(7) A payback-year map for the CHB-VCRS with FS was developed to estimate the profit years when it replaces the non-storage SC-VCRS based on a 15-year lifetime under different electricity-price ratios.

Acknowledgement

The authors gratefully acknowledge the financial supports from the Engineering and Physical Sciences Research Council (EPSRC) of the UK (EP/T022701/1).

Appendix A

This part provides the procedure of calculation of moist air properties and the flow chart of simplified modeling of cooling tower.

The relative humidity is the ratio of the actual water vapor partial pressure in moist air and the water vapor partial pressure in moist air at saturation, can be expressed by Eq. (A1) [42]:

$$\phi = \frac{p_{\mathrm{w}}}{p_{\mathrm{ws}}} \times 100 \tag{A1}$$

where p_{w} refer to the actual air vapor pressure, kPa. p_{ws} is the air saturation vapor pressure, kPa, are calculated by Eq. (A2)

$$p_{\mathrm{ws}} = (at^3 + bt^2 + ct + \mathrm{d}) \times 0.1 \tag{A2}$$

where a, b, c and d are constants with values of [43]:

$$a = 6.6\times10^{-4}; b = 4.6\times10^{-3}; c = 4.58\times10^{-1}; d = 6.63$$

The saturation humidity ratio, W_{s}, can be calculated by Eq. (A3).

$$W_{\mathrm{s}} = 0.621945 \frac{p_{\mathrm{ws}}}{p_{\mathrm{atm}} - p_{\mathrm{ws}}} \tag{A3}$$

Similarly, the humidity ratio W, can be calculated by Eq. (A4).

$$W = 0.621945 \frac{p_{\mathrm{w}}}{p_{\mathrm{atm}} - p_{\mathrm{w}}} \tag{A4}$$

The moist air specific enthalpy in kJ/kg then becomes:

$$h = 1.006t_{db} + W(2501 + 1.86t_{db}) \tag{A5}$$

The wet-bulb temperature can be determined by Eq. (A6).

$$t_{wb} = t_{db} - \frac{p_{ws}(t_{wb}) - (\phi/100)p_{ws}(t_{db})}{kp_{atm}} \tag{A6}$$

where k is a constant, p_{atm} is the atmospheric pressure and $p_{ws}(t_{wb})$ and $p_{ws}(t_{db})$ are the air saturation vapor pressure at t_{wb} and t_{db} respectively.

$$k = 6.53 \times 10^{-4}$$

Figure A1 presents the flow chart of the iterative method to determine the wet-bulb temperature by Eqs. (A2) and (A6).

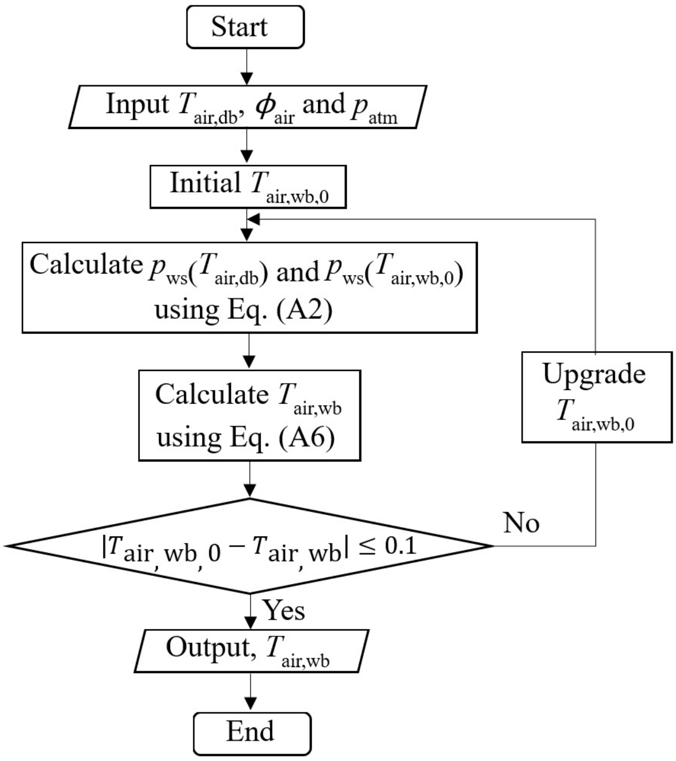

Figure A1 Flowchart of wet-bulb temperature iteration

Figure A2 presents the flowchart of modeling of the direct contact cooling tower as follow.

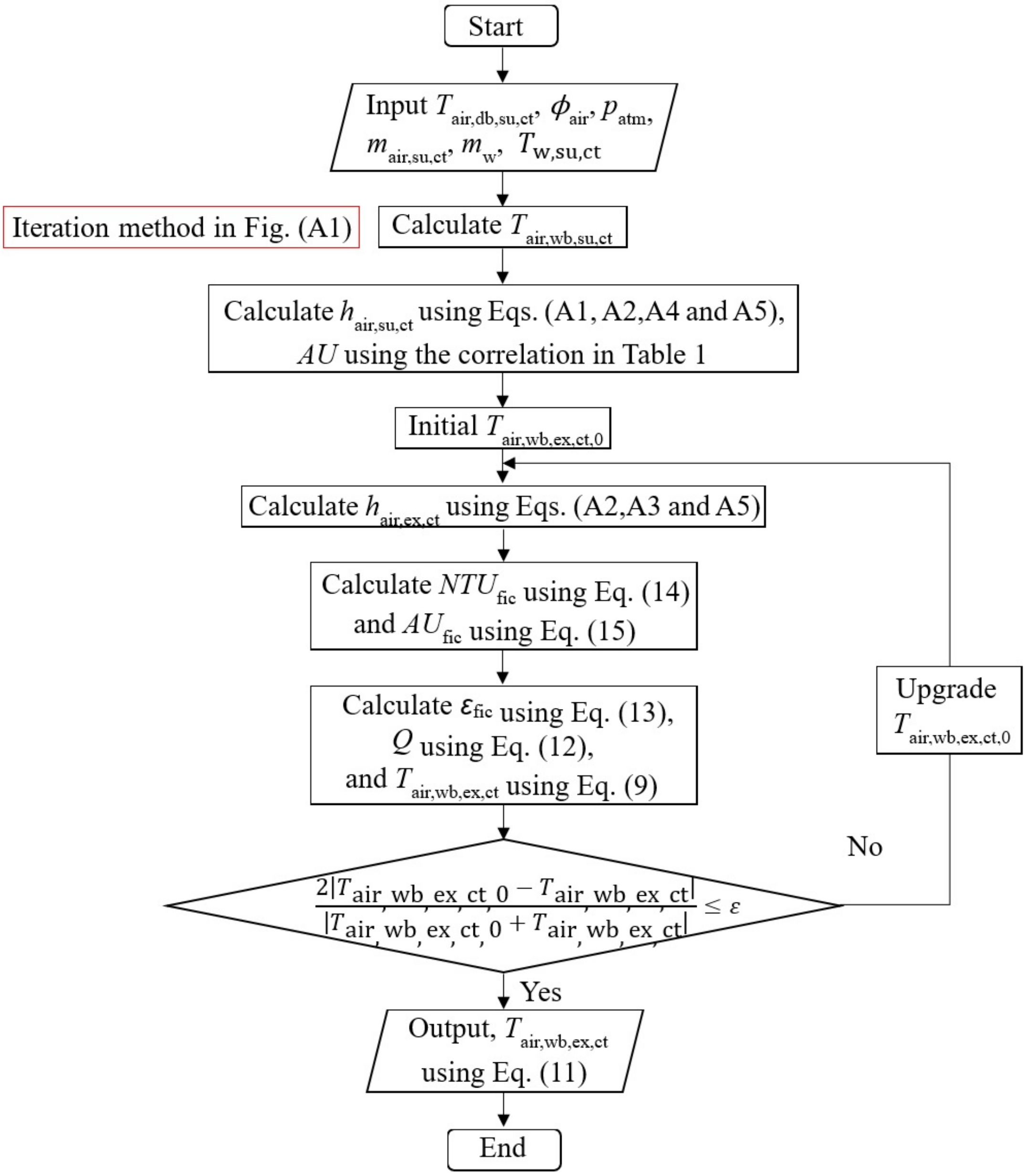

Figure A2 Flowchart of modeling of direct contact cooling tower

Appendix B

This part presents the flowchart of heat transfer calculation in a segment of gas cooler. Figure B1 is a simplified procedure and focus on presenting the main iterations during the process.

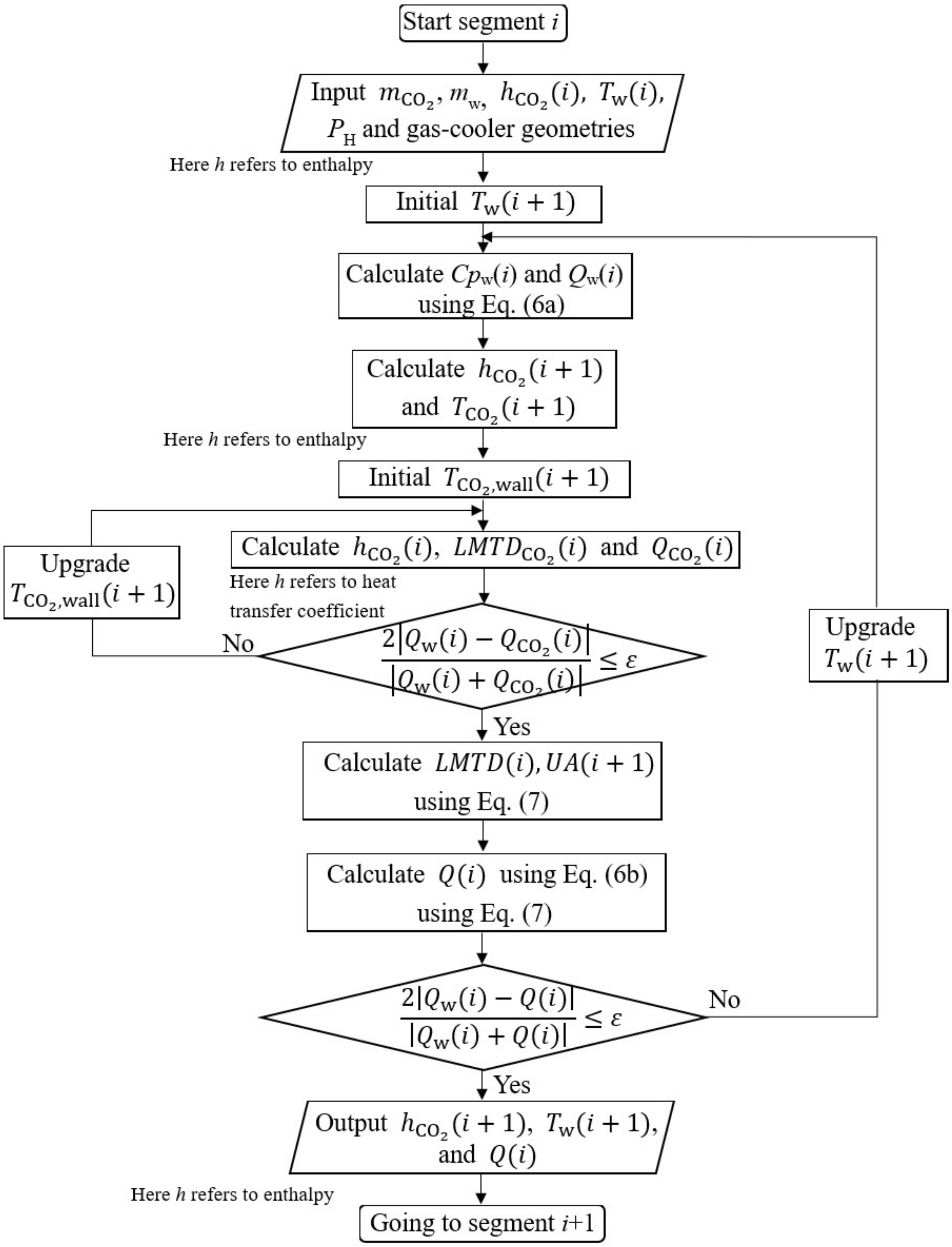

Figure B1 Flowchart of heat transfer calculation in a segment

Appendix C

This part gives the flowchart of modeling of single-stage CO_2 vapor-compression refrigeration system with variable-speed compressor.

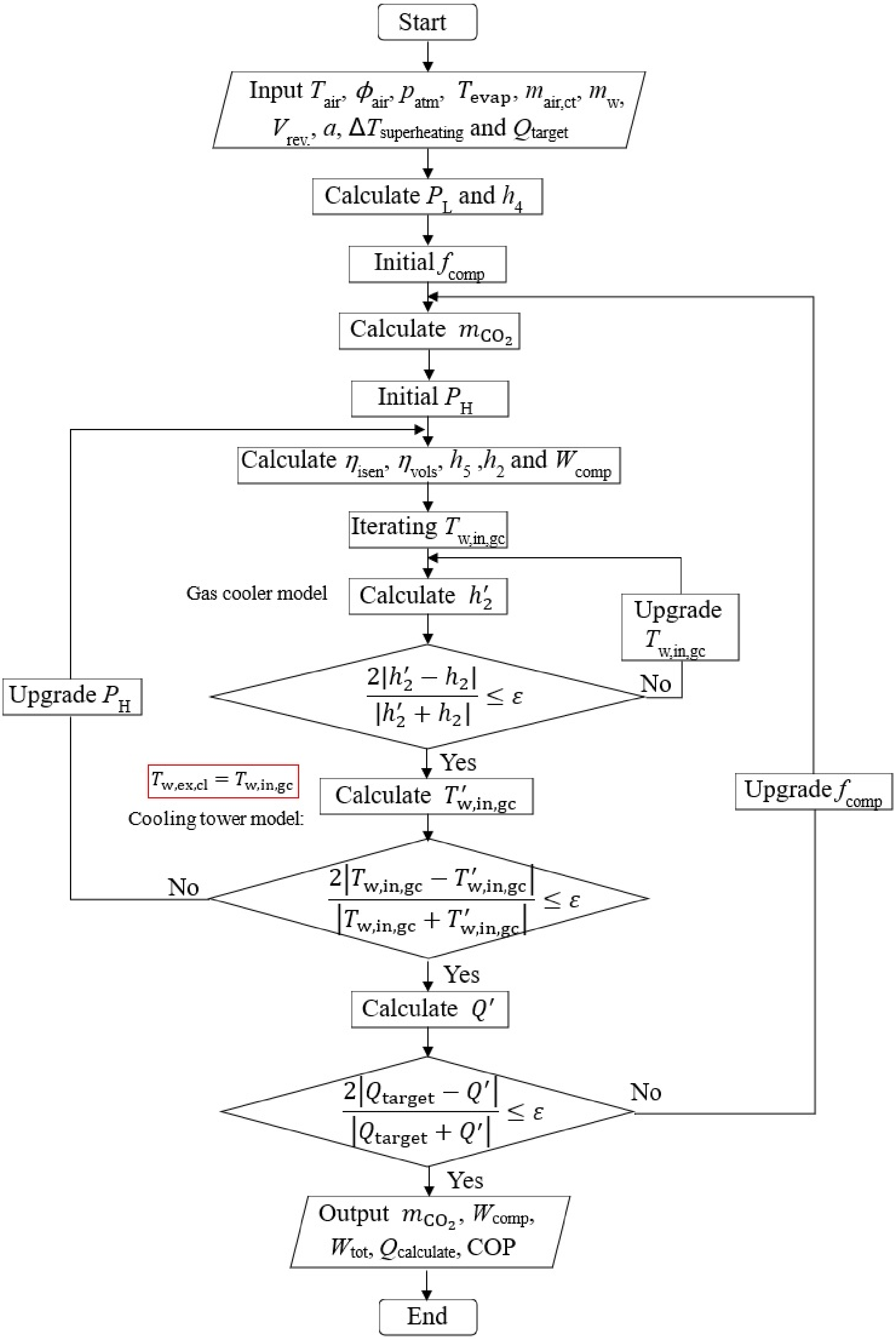

886 Figure C1 Flowchart of modelling of SC-VCRS (baseline)

887

References

1. D. Coulomb, J.L. Dupont, A. Pichard, The Role of Refrigeration in the Global Economy-29, Informatory Note on Refrigeration Technologies, 2015.
2. A.H. Mosaffa, L.G. Farshi, C.A.I. Ferreira, M.A. Rosen, Advanced exergy analysis of an air conditioning system incorporating thermal energy storage. Energy, 77 (2014) 945-952. https://doi.org/10.1016/j.energy.2014.10.006.
3. A. Delahaye, L. Fournaison, D. Dalmazzone, Use of Hydrates for Cold Storage and Distribution in Refrigeration and Air-Conditioning Applications. Gas Hydrates 2: Geoscience Issues and Potential Industrial Applications, (2018) 315-358. https://doi.org/10.1002/9781119451174.ch15.
4. Y.H. Mori, T. Mori, Characterization of gas hydrate formation in direct-contact cooling storage process, Int. J. Refrig., 12 (1989) 259-265. https://doi.org/10.1016/0140-7007(89)90091-1.
5. T. Ogawa, T. Ito, K. Watanabe, K.I. Tahara, R. Hiraoka, J.I. Ochiai, Y.H. Mori, Development of a novel hydrate-based refrigeration system: A preliminary overview, Appl. Therm. Eng., 26(17-18) (2006) 2157-2167. https://doi.org/10.1016/j.applthermaleng.2006.04.003.
6. P. Skovborg, P. Rasmussen, Comments on: Hydrate dissociation enthalpy and guest size, Fluid Phase Equilib., 96 (1994) 223-231. https://doi.org/10.1016/0378-3812(92)85082-J.
7. R. Matsuura, K. Watanabe, Y. Yamauchi, H. Sato, L.J. Chen, R. Ohmura, Thermodynamic analysis of hydrate-based refrigeration cycle, Energy, 220 (2021) 119652. https://doi.org/10.1016/j.energy.2020.119652.
8. A. Delahaye, L. Fournaison, D. Dalmazzone, Use of Hydrates for Cold Storage and Distribution in Refrigeration and Air-Conditioning Applications. Gas

Hydrates 2: Geoscience Issues and Potential Industrial Applications, 2018.

9. W. Zhang, Y. Wang, X. Lang, S. Fan, Performance analysis of hydrate-based refrigeration system, Energy Convers. Manag., 146 (2017) 43-51. https://doi.org/10.1016/j.enconman.2017.04.091.

10. N. Xie, C. Tan, S. Yang, Z. Liu, Conceptual Design and Analysis of a Novel CO_2 Hydrate-Based Refrigeration System with Cold Energy Storage, ACS Sustain. Chem. Eng., 7(1) (2018) 1502-1511. https://doi.org/10.1021/acssuschemeng.8b05255.

11. Q. Sun, Y.T. Kang, Review on CO_2 hydrate formation/dissociation and its cold energy application, Renew. Sust. Energ. Rev., 62 (2016) 478-494. https://doi.org/10.1016/j.rser.2016.04.062.

12. A. P. Roskilly, P. C. Taylor, J. Yan, Energy storage systems for a low carbon future-in need of an integrated approach, Appl. Energy, 137 (2015) 463-466. https://doi.org/10.1016/j.apenergy.2014.11.025.

13. H. Zhou, I.E.E. De Sera, C.A. Infante Ferreira, Modelling and experimental validation of a fluidized bed based CO_2 hydrate cold storage system, Appl. Energy, 158 (2015) 433-445. https://doi.org/10.1016/j.apenergy.2015.08.092.

14. B. Dai, X. Zhao, S. Liu, Q. Yang, D. Zhang, Y. Gao, Y. Hao, Heating and cooling of residential annual application using DMS transcritical CO_2 reversible system and traditional solutions: An environment and economic feasibility analysis, Energy Convers. Manag., 210 (2020) 112714. https://doi.org/10.1016/j.enconman.2020.112714.

15. B. Dai, H. Qi, W. Dou, S. Liu, D. Zhang, H. Yang, V. Nian, Y. Hao, Life cycle energy, emissions and cost evaluation of CO_2 air source heat pump system to replace traditional heating methods for residential heating in China: System

configurations, Energy Convers. Manag., 218 (2020) 112954. https://doi.org/10.1016/j.enconman.2020.112954.

16. B. Dai, H. Qi, S. Liu, Z. Zhong, H. Li, M. Song, M. Ma, Z. Sun, Environmental and economical analyses of transcritical CO_2 heat pump combined with direct dedicated mechanical subcooling (DMS) for space heating in China, Energy Convers. Manag., 198 (2019) 111317. https://doi.org/10.1016/j.enconman.2019.01.119.
17. E. Torrella, J.A. Larumbe, R. Cabello, R. Llopis, D. Sanchez, A general methodology for energy comparison of intermediate configurations in two-stage vapour compression refrigeration systems, Energy, 36(7) (2011) 4119-4124. https://doi.org/10.1016/j.energy.2011.04.034.
18. C. Dang, E. Hihara, In-tube cooling heat transfer of supercritical carbon dioxide. Part 1. Experimental measurement, Int. J. Refrigeration, 27(7) (2004) 736-747. https://doi.org/10.1016/j.ijrefrig.2004.04.018.
19. V. Gnielinsk, New equation for heat and mass transfer in turbulent pipe and channel flow, Int. Chem. Eng., 16 (1976) 359-368.
20. J. Lebrun, C.A. Silva, Cooling tower--model and experimental validation. ASHRAE Transactions, 108 (2002) 751.
21. Y. Hwang, B.H. Kim, R. Radermacher, Boiling heat transfer correlation for carbon dioxide, Science et technique du froid, (1997) 81-95.
22. ASHRAE, ASHRAE Handbook Fundamentals (SI Edition). Refrigeration and Air Conditioning Engineering Edition of the American Society of Heating, 1989.
23. C.C Wang, K.Y. Chi, C.J. Chang, Heat transfer and friction characteristics of plain fin-and-tube heat exchangers, part II: Correlation, Int. J. Heat Mass Transf., 43(15) (2000) 2693-2700. https://doi.org/10.1016/S0017-

9310(99)00333-6.

24. ASHRAE (1997), ASHRAE handbook: fundamentals, Chapter 16. Atlanta: American Society of Heating, Refrigerating and Air-Conditioning Engineers, Inc.

25. J. Lebrun, C.A. Silva, F. Trebilcock, E. Winandy, Simplified models for direct and indirect contact cooling towers and evaporative condensers, Build Serv. Eng. Res. Technol., 25(1) (2004) 25-31. https://doi.org/10.1191/0143624404bt088oa.

26. A. Nguyen, P. Eslami-Nejad, A transient coupled model of a variable speed transcritical CO_2 direct expansion ground source heat pump for space heating and cooling, Renew. Energy, 140 (2019) 1012-1021, https://doi.org/10.1016/j.renene.2019.03.110.

27. A.T. Diaby, P. Byrne, T. Mare, Simulation of heat pumps for simultaneous heating and cooling using CO_2, Int. J. Refrig., 106 (2019) 616-627. https://doi.org/10.1016/j.ijrefrig.2019.03.010.

28. J. Oignet, H.M. Hoang, V. Osswald, A. Delahaye, L. Fournaison, P. Haberschill, Experimental study of convective heat transfer coefficients of CO2 hydrate slurries in a secondary refrigeration loop, Appl. Therm. Eng., 118 (2017) 630-637. https://doi.org/10.1016/j.applthermaleng.2017.02.117.

29. J.K. Kim, L. Savulescu, R. Smith, Design of cooling systems for effluent temperature reduction, Chem. Eng. Sci., 56(5) (2001) 1811-1830. https://doi.org/10.1016/S0009-2509(00)00541-8.

30. R. F. Pontes, W. M. Yamauchi, E. K. Silva, Analysis of the effect of seasonal climate changes on cooling tower efficiency, and strategies for reducing cooling tower power consumption, Appl. Therm. Eng., 161 (2019) 114148. https://doi.org/10.1016/j.applthermaleng.2019.114148.

31. G.B. Wang, X.R. Zhang, Thermoeconomic optimization and comparison of the simple single-stage transcritical carbon dioxide vapor compression cycle with

different subcooling methods for district heating and cooling, Energy Convers. Manag., 185 (2019) 740-757. https://doi.org/10.1016/j.enconman.2019.02.024.

32. S. Khanmohammadi, M. Goodarzi, S. Khanmohammadi, H. Ganjehsarabi, Thermoeconomic modeling and multi-objective evolutionary-based optimization of a modified transcritical CO_2 refrigeration cycle, Therm. Sci. Eng. Prog., 5 (2018) 86-96. https://doi.org/10.1016/j.tsep.2017.10.007.
33. K.K. Singh, R. Kumar, A. Gupta, Comparative energy, exergy and economic analysis of a cascade refrigeration system incorporated with flash tank (HTC) and a flash intercooler with indirect subcooler (LTC) using natural refrigerant couples, Sustain. Energy Technol. Assess., 39 (2020) 100716. https://doi.org/10.1016/j.seta.2020.100716.
34. S. Sanaye, A.Shirazi, Thermo-economic optimization of an ice thermal energy storage system for air-conditioning applications, Energy and Build., 60 (2013) 100-109. https://doi.org/10.1016/j.enbuild.2012.12.040.
35. C.S. Park, Fundamentals of Engineering Economics, second ed., Pearson/Prentice Hall, Upper Saddle River, NJ, 2008.
36. D.O. Lee, Urban—rural humidity differences in London, Int. J. Climatol., 11(5) (1991) 577-582. https://doi.org/10.1002/joc.3370110509.
37. University of Wisconsin, TRNSYS 17: A transient system simulation program, Solar Energy Laboratory 2010.
38. UKPower, Everything you need to know about Economy 7, https://www.ukpower.co.uk/home_energy/economy-7.
39. Ministry of Housing, Communities & Local Government, English Housing Survey, published on 10 Jul. 2013, last updated on 17 Dec. 2020, https://www.gov.uk/government/collections/english-housing-survey.

40. R. Dott, M.Y. Haller, J. Ruschenburg, F. Ochs, J. Bony, The Reference Framework for System Simulations of the IEA SHC Task 44 / HPP Annex 38—Part B: Buildings and Space Heat Load, A technical report of subtask C—Report C1 Part B, International Energy Agency, 2013, http://task44.iea-shc.org/Data/Sites/1/publications/T44A38_Rep_C1_B_ReferenceBuildingDescription_Final_Revised_130906.pdf
41. B. Silvertti, Application fundamentals of ice-based thermal storage, ASHRAE Journal, 44 (2002) 30-35.
42. ASHRAE (2009), ASHRAE handbook: fundamentals, Atlanta: American Society of Heating, Refrigerating and Air-Conditioning Engineers, Inc.
43. A.T. Martinez, On the evaluation of the wet bulb temperature as a function of dry bulb temperature and relative humidity, Atmosfera, 7 (1994) 197-184.